

11-10-12
0517
34836**Final Report****Studies on Equatorial Shock Formation
During Plasmaspheric Refilling****Grant # NAGW-2128****P.I.: Dr. N. Singh**

During the grant period from August 1, 1994 to October 31, 1995 we have continued to investigate the effects of plasma wave instabilities on the early stage plasmaspheric refilling. Since ion beams are the primary feature of the interhemispheric plasma flows during the early stage refilling, ion-beam driven instabilities and associated waves are of primary interest. The major findings of this research are briefly summarized here. After a systematic examination of the relevant plasma instabilities, we realized that when the interhemispheric plasma flows begin to interpenetrate at the equator, the most relevant plasma instability is the electrostatic ion cyclotron wave instability. Only at later stages the ion-acoustic instability may be affecting the plasma flow. An interesting property of the electrostatic ion cyclotron wave is that it heats ions perpendicular to the magnetic field. When the ions in the field-aligned flows are transversely heated, they are trapped in the magnetic flux tube, thus affecting the refilling process.

The eic wave instability is a microprocess with scale length of the order of ion Larmor radius and the corresponding time scale is the ion cyclotron period. On the other hand, the refilling is a mesoscale process. The coupling of micro- and mesoscale plasma processes in space plasma transport has remained an unsolved challenging problem in space physics. We have attempted to tackle this problem for the plasmaspheric refilling by incorporating the effects of eic wave instability on the mesoscale plasma flow when the properties of the latter exceeds the critical (marginal) conditions for the former. We have incorporated the eic wave effects in a mesoscale semikinetic model, which is based on a one-dimensional particle-in-cell code for the interhemispheric plasma flow along closed magnetic field lines.

We have compared the results on refilling from the model with and without the eic instability effects. The model with eic instability reveals that when the interpenetrating ion beams drive eic waves in the equatorial region the perpendicularly heated ions spread all over the flux tube creating two distinct ion populations consisting of (1) counterstreaming field-aligned ion beams, and (2) warm anisotropic ions with pitch angle distribution peaking at 90° . The latter population is highly anisotropic at the equator and its ions have energies up to a few tens of eV . Such equatorially trapped ion population has been measured by satellites [Olsen, 1981; Olsen *et al*, 1987]. However, most explanations for the generation of this ion population involve external waves driven by the hot protons of the magnetospheric origin. Since hot protons drive fast waves which do not resonate with the cold ions in the interhemispheric flow, there is a difficulty with such an explanation. In the model presented here the eic waves affecting the perpendicular ion heating are generated by the interhemispheric plasma flows themselves. The eic waves facilitate in transferring the parallel energy in the flow into perpendicular energy. The forerunner ions in the expanding ionospheric plasma during the early stage of the interhemispheric flow after a geomagnetic storm have sufficiently large parallel energies to produce the trapped ions having energies up to a few tens of eV .

The results from our model also explains the observation that the warm anisotropic population with pitch angle distribution peaking at 90° is not limited to the equatorial region, but it extends to off-equatorial regions at large geomagnetic latitudes. Sojka *et al* [1983] have reported simultaneous measurements of different ion populations in off-equatorial regions on flux tubes undergoing refilling. These populations typically include (1) a thermal isotropic ion population with a few eV energy, (2) field-aligned flows with double or single streams, and (3) warm anisotropic ions with pitch angle distributions peaking at 90° . Our present model with eic waves yields the latter two populations. In order to produce the thermal isotropic population, we need to further extend our semikinetic model to include Coulomb collisions. We hope to continue this effort if the research grant is continued.

Recent Publications

1. N. Singh and L. W. Leung, Numerical simulation of filling a magnetic flux tube with a cold plasma: Anomalous plasma effects, *J. Geophys. Res.*, *100*, 3585, 1995.
2. N. Singh, Effects of electrostatic ion cyclotron wave instability on plasma flow during early stage plasmaspheric refilling, Submitted to *J. Geophys. Res.*, Nov. 1995.
3. N. Singh and L. W. Leung, Numerical simulation of an injection of a hot plasma in the counterstreaming interhemispheric flow, Paper being prepared for *J. Geophys. Res.*

Numerical simulation of filling a magnetic flux tube with a cold plasma: Anomalous plasma effects

Nagendra Singh and W. C. Leung

Department of Electrical and Computer Engineering and Center for Space Plasma and Aeronomic Research
University of Alabama in Huntsville

Abstract. Large-scale models of plasmaspheric refilling have revealed that during the early stage of the refilling counterstreaming ion beams are a common feature. However, the instability of such ion beams and its effect on refilling remain unexplored. The difficulty with investigating the effect of ion-beam-driven instability on refilling is that the instability and the associated processes are so small-scale that they cannot be resolved in large-scale models. Typically, the instabilities have scale lengths of a few tens of plasma Debye length, which is a few meters at the most, and the spatial resolution in large-scale models is at least several tens of kilometers. Correspondingly, the temporal scale of the instability is by several orders of magnitude smaller than the temporal resolution afforded by the models. In order to learn the basic effects of ion beam instabilities on refilling, we have performed numerical simulations of the refilling of an artificial magnetic flux tube. The shape and size of the tube are assumed so that the essential features of the refilling problem are kept in the simulation and at the same time the small-scale processes driven by the ion beams are sufficiently resolved. We have also studied the effect of commonly found equatorially trapped warm and/or hot plasma on the filling of a flux tube with a cold plasma. When the warm and/or hot plasma consists of anisotropic ions and isotropic electrons, the potential barrier set up by this plasma has a drastic effect on the flow of the cold ion beams, and hence on the filling. Three types of simulation runs have been performed. In run 1 we have only a cold plasma and we treat ions kinetically and electrons are assumed to obey the Boltzmann law. In run 2 both electrons and ions in the cold plasma are treated kinetically. Run 3 is similar to run 2, but it includes an equatorially trapped plasma population as mentioned above. A comparison between the results from run 1 and run 2 reveals that in the latter type of simulation electron-ion (e-i) and ion-ion (i-i) instabilities occur and significantly modify the evolution of the plasma density distributions in the flux tube along with the total plasma content. When the electron dynamics is simplified by the assumption of the Boltzmann law, both the electron-ion and ion-ion instabilities are inhibited. On the other hand, when electrons are treated kinetically, the e-i instability occurs at an early stage when ion beams are too fast to excite the i-i instability. The former instability heats the electrons so that conditions for the latter instability are eventually met. The i-i instability and its nonlinear evolution creates potential structures which significantly modify the filling process. In run 2 filling is enhanced over run 1 due to the trapping of the plasma in the potential structures. Run 3 with the equatorially trapped plasma consisting of hot anisotropic ions and warm isotropic electrons shows that the difference in the thermal anisotropy between electrons and ions generates electrostatic shocks in the flow of the initially fast ion beams. The propagating shocks yield extended potential structure in the flux tube. The trapping of plasma in the potential structure further enhances the filling in run 3 over that seen in run 2.

1. Introduction

An outstanding problem in space plasma transport is the coupling of microscale and mesoscale processes. An interesting example of this problem is the early stage refilling of the outer plasmaspheric flux tubes after geomagnetic storms. The plasma evacuation from the flux tubes for magnetic shell $L > 3$ during the disturbed times creates pressure gradients between the ionosphere and the equatorial region, driving highly supersonic ion beams in the interhemispheric plasma flow. The

counterstreaming ion beams should be able to drive instabilities and affect the plasma flow and hence the refilling process.

The renewed theoretical effort on plasmaspheric refilling during the last 10 years or so has been primarily on large-scale modeling using hydrodynamic [Khazanov *et al.*, 1984; Singh *et al.*, 1986; Rasmussen and Schunk, 1982; Singh, 1988, 1990, 1991a; Guiter and Gombosi, 1990; Singh and Chan, 1992] and semikinetic [Wilson *et al.*, 1992; Lin *et al.*, 1992] treatments. The temporal and spatial resolutions afforded by the model are generally too crude to include the microscopic effects. Driven by the idea that interpenetrating ion beams may generate shocks during refilling [Banks *et al.*, 1971], the physics of shock formation has been studied using small-scale simulations [Singh and Schunk, 1983; Singh *et al.*, 1986; Singh, 1988; Singh and Chan, 1992]. More recently some anomalous effects in terms of

transverse ion heating and scattering of ions have been included in the theoretical studies of the refilling problem, but these effects are not directly driven by the ion beams. Instead it is hypothesized that the heating and scattering is caused by waves generated by a hot plasma trapped in the equatorial region [Singh *et al.*, 1982; Singh and Hwang, 1987; Singh and Torr, 1990; Singh, 1991b; Singh and Chan, 1992; Lin *et al.*, 1992].

The main purpose of this paper is to study the effect of ion-beam-driven waves on the filling of a magnetic flux tube with plasma flowing into it from its ends, as schematically shown in Figure 1a. Since we wish to resolve the microprocesses associated with the instability caused by the ion beams, we cannot model an entire plasmaspheric flux tube. Therefore we perform the study by means of numerical simulations of plasma flow in an artificial flux tube, which has the essential feature of magnetic mirrors. Owing to the limited size of the flux tube included in the simulation, results presented here illustrate the basic properties of the ion-beam-driven instabilities, their effects on the plasma flow and the accumulation of the plasma in the tube. These results cannot be quantitatively applied to a plasmaspheric flux tube, but the basic ideas found here are applicable and the question is raised as to how to include them in the large-scale refilling models. However, no attempt has been made to answer this question in this paper.

The basic ideas found from the simulation on ion-beam-driven instabilities are as follows. When the simulation is performed by treating ions kinetically and electrons by simply assuming that they obey the Boltzmann law (run 1), the ion-beam-driven instabilities are not found because the beams are too fast to excite the waves in a one-dimensional plasma. On the other hand in run 2, in which electrons are also treated kinetically, the fast ion beams during the early stage of the evolution of the plasma in the flux tube drive electron-ion instability [Fujita *et al.*, 1977; Singh, 1978]. This instability contributes to the heating of electrons in conjunction with the electron energization in the self-consistent potential distributions resulting from counterstreaming plasma expansion. This heating increases the ion acoustic speed in the plasma and

thereby the initially fast ion beams eventually become slow enough relative to the ion acoustic speed to drive the ion-ion instability, which is found to be very effective in coupling counterstreaming ion beams and in trapping of plasma in the flux tube, especially in its outer regions away from the central minimum magnetic field (Figure 1b). Comparing the results from the simulations with and without the kinetic treatment of the electrons, we found that in the former simulation the filling of the flux tube is enhanced due to the trapping of plasma in the potential structures set up by the ion-ion instability. The instability also drives electrostatic shocks and distributes the plasma in the flux tube quite differently from that in the simulation with the simplified electron dynamics. Furthermore, this instability controls the influx of ions into the central region of the flux tube, and thereby the dynamics of the potential structures including the electrostatic shocks in the central region.

We further extend this study by including a hot plasma population trapped in the central region of the flux tube where the magnetic field is minimum as shown in Figures 1a and 1b. We refer to this simulation study as run 3. This study is motivated by the fact that the outer region of the plasmasphere is always populated by a hot plasma of plasma sheet and the ring current origins [Roux *et al.*, 1982; Deforest *et al.*, 1971]. Furthermore, at times a warm plasma population is created when cold ions in the equatorial region are transversely heated by waves generated by the hot plasma population [Olsen *et al.*, 1987]. How do these warm and/or hot plasma populations affect the flow of cold plasma and the refilling of the plasmasphere? In a previous paper [Singh, 1993] we reported that the presence of an equatorially hot plasma, consisting of hot anisotropic ions and warm electrons, has drastic effects on the flow and evolution of the initially fast ion beams developing in an empty flux tube. The difference in the thermal anisotropies of the hot ions and warm electrons sets up a sufficiently large potential barrier for the ions; this causes reflection of the ion beams and shock formations. When shocks propagate away from the trapped plasma, an extended potential structure develops covering the entire flux tube. We report here that such a potential structure further enhances the refilling over that seen in run 2 without the trapped plasma.

The rest of the paper is planned as follows: in section 2 we describe the numerical technique. In section 3 numerical results from run 1 and run 2 dealing with the ion-beam-driven instabilities are described along with their interpretation. Section 4 contains the discussion on results from run 3 in which the equatorially trapped hot plasma is included. In section 5, we have compared the flux tube filling as seen from different simulations. The conclusion of the paper is given in section 6.

2. Numerical Model

We perform a one-dimensional particle-in-cell simulation of plasma flow along an artificial flux tube (Figure 1a). The magnetic field $B(x) = B_0(1 - \alpha \exp(-(x-d/2)^2/\sigma^2))$ where B_0 is a constant field outside the minimum-field region (Figure 1b), d is the size of the simulation system and the choice of α and σ determines the desired field distribution. The cold plasma flows into the flux tube from the two plasma reservoirs at the ends of the simulation system at $x=0$ and $x=d$ (Figure 1a). The simulation technique is described by Singh and Chan [1992]. Plasma dynamics is simulated using a particle-in-cell (PIC) code. We have performed two types of

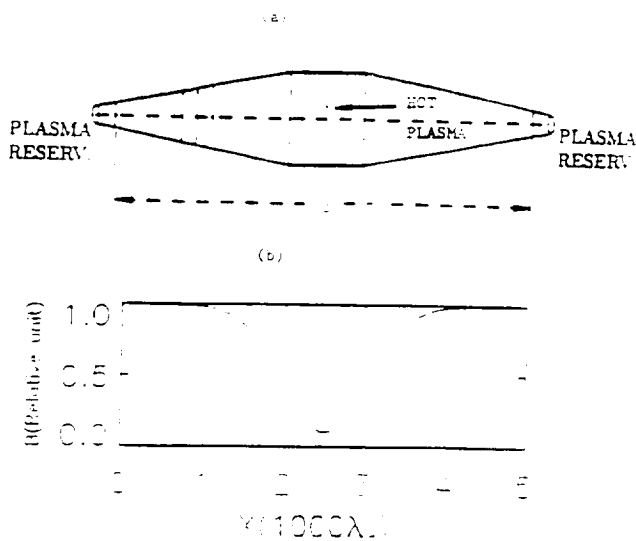


Figure 1. (a) Geometry of the simulation: the magnetic flux tube and the two plasma reservoirs at the ends of the tube are shown. The flux tube fills with plasma when the plasmas from the reservoirs expand into it. (b) Magnetic field distribution in the flux tube: the mirror ratio is 1.

simulations dealing with the cold plasma flow into the flux tube: in one type, called here run 1, ions are treated kinetically using the PIC code while electrons are assumed to obey the Boltzmann law. This assumption along with the assumed condition of a quasi-neutral plasma gives the electric field $E = -(kT_e / en_i) dn_i / dx$ where n_i is the ion density, k is the Boltzmann constant, and T_e is the electron and ion temperatures in the plasma reservoirs. In the other type of simulation, called run 2 here, both electrons and ions are treated kinetically using the PIC code and we solve the Poisson equation for the electric field with the boundary conditions $\phi(x=0) = \phi(x=d) = 0$, where $\phi(x)$ denotes the potential distribution. As the particles move in the flux tube, their magnetic moments are assumed to be conserved.

The velocity distribution function of the ions and electrons in the plasma reservoir is assumed to be Maxwellian with a temperature T_0 . The reservoirs supply a continuous flux of charged particles into the flux tube through the process of plasma expansion. In the simulations reported here, we have used $m_i / m_e = 400$, which adequately separates the electron and ion time scales and, at the same time, allows computationally feasible runs. Numerical parameters of the simulations are as follows: system size $d = 5 \times 10^3 \lambda_d$, the magnetic field parameters $\alpha = 0.9$, and $\sigma = 750 \lambda_d$ for which $B(x)$ is plotted in Figure 1b, cell size $\Delta x = 20 \lambda_d$, and time step $\Delta t = 0.1 \omega_{pe0}^{-1}$, where λ_d and ω_{pe0} are the Debye length and electron-plasma frequency in the cold plasma reservoirs, respectively. In the following discussion we have used normalized quantities defined as follows: time $\bar{t} = t \omega_{pi0}$, distance $\bar{x} = x / \lambda_d$, velocity $\bar{V} = V / V_{te}$ and electric potential $\bar{\phi} = e\phi / kT_0$, where $V_{te} = (kT_0 / m_e)^{1/2}$, $\omega_{pi0} = (m_e / m_i)^{1/2} \omega_{pe0}$.

We also performed a simulation, called here run 3, by including an initial hot plasma in the central region of the flux tube determined by $2300 \leq x / \lambda_d \leq 2700$. The hot plasma consists of hot anisotropic ions and warm isotropic electrons; details of the hot plasma properties are given in section 4.

3. Flux Tube Filling and Ion-Beam-Driven Instabilities

In this section we examine the evolution of the plasma and the potential distributions in the flux tube as seen from run 1 and run 2. A comparison of results from these runs reveal when and why plasma instabilities are excited and how they affect the plasma and field distributions.

Figure 2 shows the evolution of the ion phase space in $\bar{x} - \bar{V}_{\parallel}$ plane from run 1. Note that the velocity on the vertical axis is measured in units of the ion thermal velocity $V_{te} = (kT_0 / m_i)^{1/2}$. Figure 2a for $\bar{t} = 200$ shows the expanding ion beams from the two plasma sources shown in Figure 1a. By the time $\bar{t} = 10^3$ (Figure 2b) the counterstreaming of ion beams is set up all along the flux tube; the counterstreaming continues without a significant interaction between the beams as seen from Figures 2c and 2d for $\bar{t} = 2000$ and 4000, respectively. The main feature of the spatial evolution of the ion beams is that they progressively slow down as they approach the opposite end of the flux tube. From the plot at $\bar{t} = 4000$, we also note that a few particles in the ion beams approaching the opposite ends slow down up to almost zero velocity; the number of such ions increases with time as seen from the plots at $\bar{t} = 8000$. This tends to slowly fill in the velocity space between the two counterstreaming ion beams in the off-central region. We find

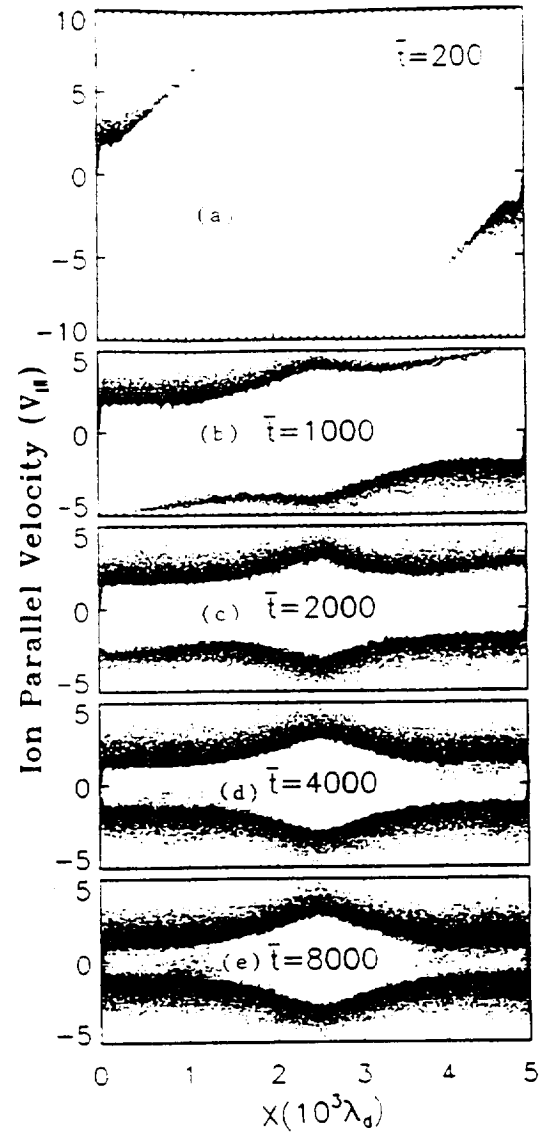


Figure 2. Evolution of ion phase space in $\bar{x} - \bar{V}_{\parallel}$ plane from run 1.

that such scattering of ions is not caused by anipolar electric fields, which are given by the ion density gradients.

The evolution of the ion density profile in the flux tube is shown in Figure 3. After the initial stage ($\bar{t} < 1000$), the density profiles are generally smooth having relatively large gradients in the central region ($(1500 < |\bar{x}| < 2500)$), and in the off-central region ($100 < \bar{x} < 1500$ and $3500 < \bar{x} < 4900$) the gradients are weak giving weak electric fields. The scattered particles in Figures 2d and 2e occur in the latter regions. In view of the weak anipolar electric fields, incapable of slowing down or reflecting the beams, we suggest that the scattering occurs via some anomalous effects involving fluctuations in the plasma. Later we discuss this issue further after we have considered the flow in run 2.

The evolution of ion phase space in $\bar{x} - \bar{V}_{\parallel}$ plane for run 2 is shown in Figures 4a to 4f. Note that in this figure the velocity is normalized with respect to V_{te} , in contrast to V_{ti} in Figure 2 for run 1. A comparison of the phase space plots in Figure 2b and Figure 4b, which are for the same time $\bar{t} = 10^3$, shows a significant difference in the topology of the distribution of the average flow velocity of ions in the two runs; in run 1 with the

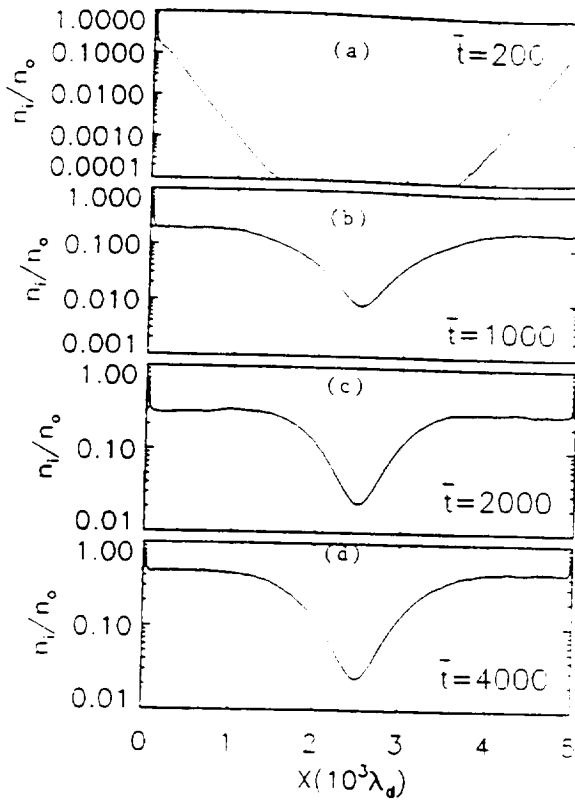


Figure 3. Plasma density distributions at some selected times from run 1.

Boltzmann electrons, the ions have relatively large velocities near $\bar{x} = \bar{x}_{mid}$ creating a "bulge" in the plots. The bulge is not seen in run 2. The bulge in Figure 2 is simply a manifestation of the magnetic field distribution $B(x)$ (Figure 1b), which controls the density distribution and hence the potential distribution according to the Boltzmann law. The relatively sharp density gradients in the density distribution on either side of the midpoint yield relatively large electric fields, which accelerate ions coming into the central region and then decelerates them while leaving. On the other hand, in run 2 the Poisson equation including a self-consistent treatment of the space charges does not yield a potential distribution controlled by $B(x)$. The potential distributions for run 2 are shown in Figures 4g to 4l.

In run 1 we saw only a weak scattering of the beam ions at late times ($\bar{t} \geq 4000$) into the velocity region between the two counterstreaming beams outside the central region of the simulation region. In contrast, in run 2 we find that wave-particle interactions plays a significant role in coupling and mixing the counterstreaming ion beams. This can be seen from the phase space plots for $\bar{t} \geq 1400$ in Figures 4c to 4f. The plot at $\bar{t} = 1400$ shows that ion-ion instability has occurred outside the central region and it is sufficiently strong to locally couple the ion beams. The instability is more clearly manifested in the potential plots given in Figures 4g to 4l. The corresponding electron phase space plots are shown in Figures 4m to 4r. Both electron and ion phase space show formation of vortices, which evolve from the ion-ion instability driven by the counterstreaming ions. We now examine in detail why this instability is so prominent in run 2, but not in run 1.

3.1. Ion-Ion Instability

The conditions for the ion-ion instability in a plasma having counterstreaming ion beams depends on a number of parameters of the beam-plasma system: these parameters are the relative beam velocity V_{br} between the two beams, the ratios of the beam temperatures T_{b1} and T_{b2} to the electron temperature T_e , and the relative densities of the ion beams n_{b1}/n_{b2} [Fried and Wong, 1966]. The relative velocity and the temperature ratios T_{b1}/T_e and T_{b2}/T_e play crucial roles in determining whether the instability occurs or not. For two symmetric counterstreaming ion beams, i.e., $V_{br} = 2V_b$, where $\pm V_b$ are the two beam velocities, and $T_{b1} = T_{b2} = T_i$, the instability occurs when [McKee, 1970]

$$1.3V_{ti} \leq V_b \leq C_s, \quad T_e > 3T_i \quad (1)$$

where C_s is the ion acoustic speed given by $C_s = (k(T_e + 3T_i)/m_i)^{1/2}$ and $V_{ti} = (kT_i/m_i)^{1/2}$.

For nonsymmetric beams it is not possible to give analytical conditions as above for the symmetric ones. However, some qualitative assessments can be made; if one of the beams is warmer than the other, say $T_{b1} > T_{b2}$, instability occurs as long as the velocity condition in (1) is met and $T_e/T_{b1} > 3$ [Baker, 1973; Gresillon and Doveil, 1975; Singh, 1978]. However, Fried and Wong [1966] have shown that when one of the beams is sufficiently cold depending on the relative beam density, the instability can occur even if the warm beam satisfies the condition $T_{b1}/T_e = 1$.

Now we examine if the instability conditions described above are met in our simulations. The instability conditions discussed above are for a Maxwellian velocity distribution, but we find that the distributions resulting from the phase space plots in Figure 2 are not Maxwellian. However, effective beam velocities and temperatures as first and second order moments of the individual ion beams can be calculated, and, as an example, they are given in Table 1 for the outer region $4000 \leq \bar{x} \leq 4500$. Note that the velocities given in this table are normalized with respect to V_b . The ion beams for $V_{||} < 0$ and $V_{||} > 0$ are called beam 1 and beam 2, respectively. The relative beam velocity $V_{br} = V_{b2} - V_{b1}$ and the ion acoustic speed are also tabulated. We find from Table 1 that the beam temperatures do satisfy the condition for the instability given by (1). However, the relative beam velocity is too large to excite the instability, that is, $V_{br} > 2C_s$; thus the ion-ion instability, as predicted from the linear instability analysis for Maxwellian ion beams, should not occur. However, as noted earlier, the beams are not Maxwellian; we find that the fall of the distribution functions at velocities below their respective peak velocities is quite sharp as shown by the inset of Figure 5. The peak separation in velocity progressively decreases from $\Delta V = 3.1$ at $\bar{t} = 4000$ to $\Delta V = 2.6$ at $\bar{t} = 8000$. Taking ΔV as V_{br} we find that the instability condition on velocity is marginally satisfied at $\bar{t} = 8000$. The approach toward the marginal instability causes an enhanced fluctuation in the plasma [Ichimaru, 1973] and the consequent scattering of ions in velocity space as mentioned earlier. Figure 5 shows evolution of the density fluctuations at $\bar{x} = 1500$ and 500 ; we note from this figure that with the decreasing distance from the end of the flux tube, the amplitude of the density fluctuation increases, and therefore the fluctuations in the electric field also increases. The fluctuation in the electric field scatters the ions, populating the velocity region between the ion beams. The scattered ions appear as a

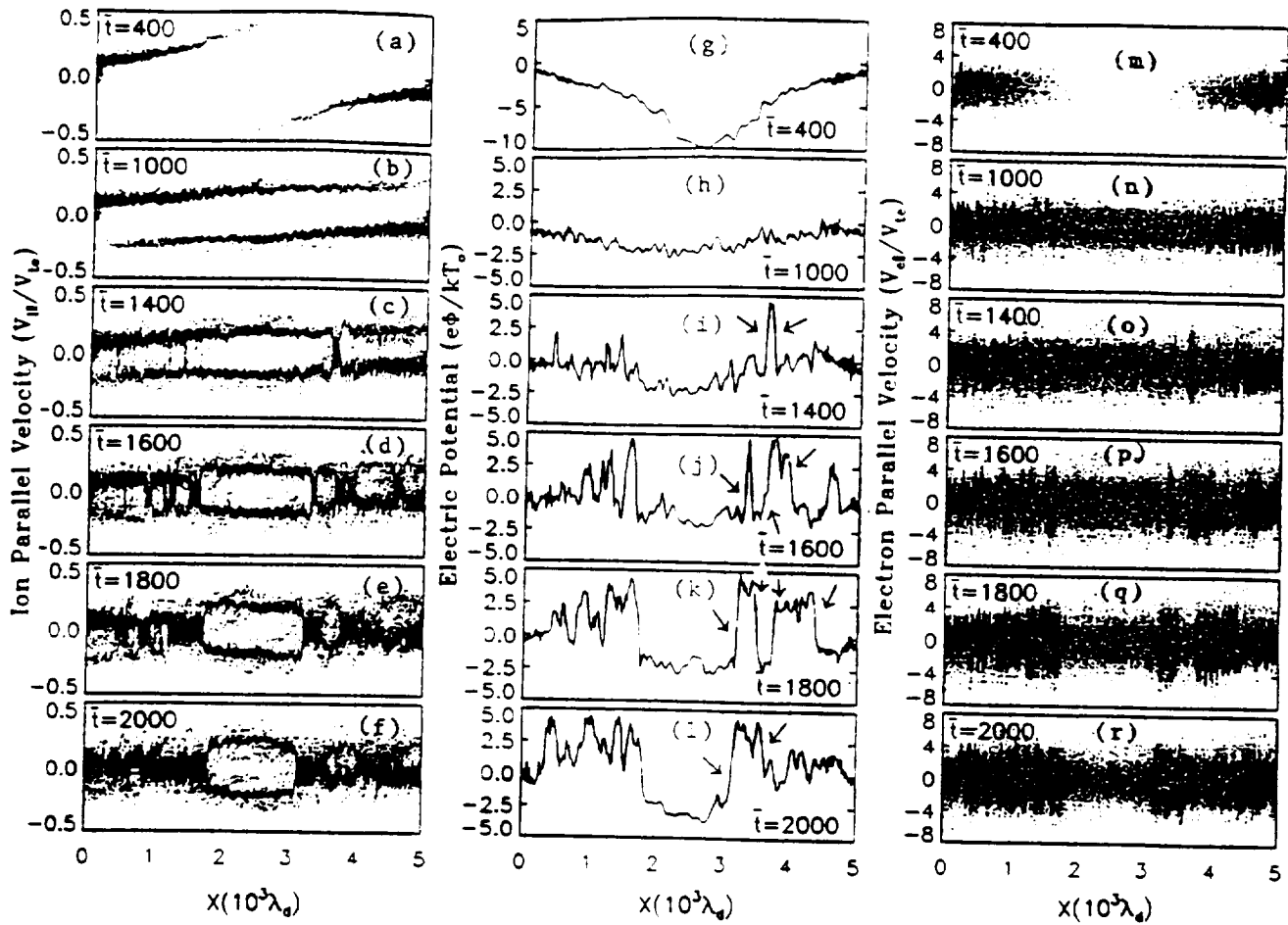


Figure 4. (a to f) Evolution of ion phase space in the $\bar{x} - \bar{V}_\parallel$ plane from run 2. Note the coupling between the ion beams due to ion-ion instability for $\bar{t} \geq 1400$. (g to l) Potential distribution corresponding to the phase space evolution in Figures 4a to 4f. The arrows in panels j, k and l show the evolution of the shock pairs from the positive potential cells created by the ion-ion instability. (m to r) Evolution of electron phase space in the $\bar{x} - \bar{V}_\parallel$ plane.

"tail" to the velocity distribution function near $V=0$. In the central region of the flux tube, where the ion beams are quite fast and far from the marginal instability condition, the fluctuations in the density and the electric fields are weak and scattering of ions is not seen (see Figure 2e).

Like Table 1 for run 1, Table 2 shows the ion beam and plasma parameters relevant for the linear instability analysis for run 2. The ion beams denoted by subscripts "1" and "2" are for $V_{\parallel 1} < 0$ and $V_{\parallel 2} > 0$, respectively. All velocities given in this table are normalized with respect to V_{te} . Comparing V_{b1} and C_s in Table 2, we find that by the time $\bar{t} = 1400$, the velocity condition on the instability is met; i.e., $V_{b1} \leq 2C_s$. We note that the temperature condition for the i-i instability is also satisfied because $T_{b1}/T_e = 0.13$ and $T_{b2}/T_e = 0.3$. Thus the instability occurs as manifested by the ion and electron phase space plots, and the potential distribution in Figure 4 for times $\bar{t} \geq 1400$.

3.2. Electron-Ion Instability

It is noted from Table 2 that in run 2 electron heating is the key for fulfilling the instability condition by increasing the ion acoustic speed; Table 2 shows that the electrons are heated to an effective temperature of $3.1T_e$ by $\bar{t} = 1400$. How are the electrons heated? We discuss here the mechanism for the electron heating.

In an ion beam-plasma system, e-i instability is yet another mechanism for exciting waves, which heats the electrons [McKee, 1970]. The e-i instability occurs when the ion beams are relatively fast [Fujita *et al.*, 1977; Singh, 1978]. This instability is kinetic, and it occurs as the slow (negative energy) wave of an ion beam undergoes Landau damping by the electrons [Hasegawa, 1975; Singh 1978]. Such an instability creates density fluctuation at frequencies less than the ion plasma frequency. In order to demonstrate that this instability does occur in run 2, we show in Figures 6a and 6b the evolution of the plasma and the potential by plotting $\bar{n}_e(t)$, $\bar{n}_i(t)$ and $\bar{\phi}(t)$ at $\bar{x} = 2500$. Figure 6a shows the evolution of the electron and ion densities. For $\bar{t} < 200$, the central region is nearly unpopulated with a plasma because the expanding plasmas from the sources at the end of the flux tube have not yet reached there. From $\bar{t} \sim 200$ to $\bar{t} \sim 400$, the central region is electron rich, and when $\bar{t} > 400$ the central region acquires a quasi-neutral plasma with $n_e \approx n_i$. The plasma density builds up to $\sim 10^{-2}n_0$ by $\bar{t} = 1000$.

The electric potential shown in Figure 6b is expected to slowly evolve with the plasma build up in response to the counterstreaming plasma expansion into the flux tube. This slow evolution is shown by a dotted-line curve, which is the potential averaged over a time interval $\Delta\bar{t} = 100$. The

Table 1. Ion Beam Parameters From Run 1

\bar{t}	\bar{n}_{b1}	\bar{n}_{b2}	V_{b1}	V_{b2}	V_{be}	\bar{T}_{b1}	\bar{T}_{b2}	\bar{T}_e	\bar{C}_e
4000	0.55	0.45	-1.60	1.85	3.45	0.16	0.18	1	1.22
6000	0.52	0.48	-1.58	1.60	3.18	0.20	0.23	1	1.30
8000	0.51	0.49	-1.51	1.51	3.00	0.21	0.27	1	1.31

fluctuations superimposed on this curve, as shown by the solid-line curve, are relevant to our discussion here. The frequency spectrum of the potential variation in Figure 6b is shown in Figure 6c. We notice that there is a broad peak in the frequency range $0.01 \leq f/f_{pe} \leq 0.1$, where f_{pe} is the ion plasma frequency in the plasma sources. For the time period of simulation shown in Figure 6, the local plasma density at $\bar{x} = 2500$ is $\bar{n} < 10^{-2} n_0$, and hence the local ion plasma frequency $f_{pi} < 0.1 f_{pe}$. Thus the low-frequency oscillations are bounded by this local plasma frequency. These low-frequency fluctuations which have amplitudes up to $4 kT_e/e$, heat the electrons to a temperature of up to $3T_e$ as shown in Table 2.

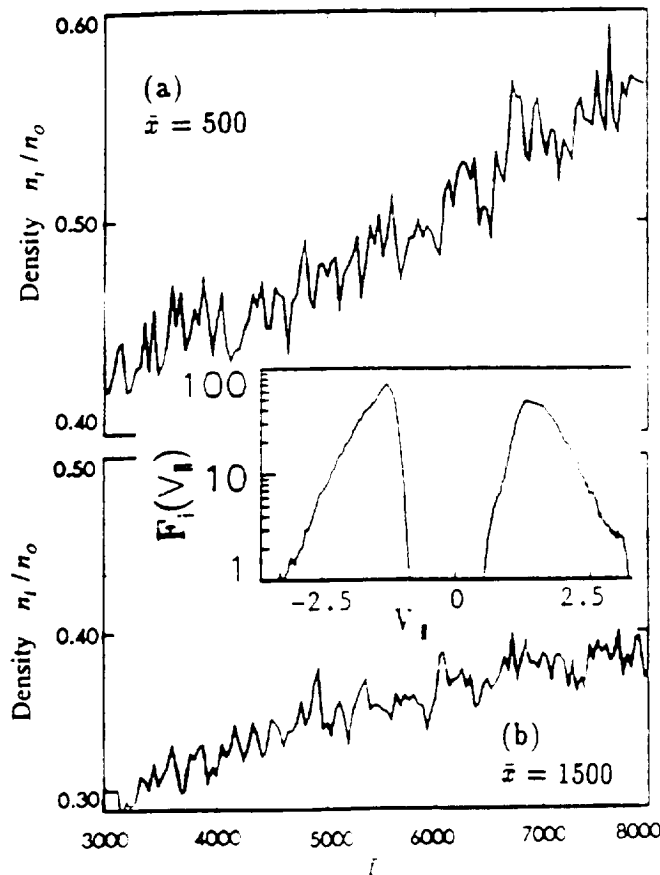


Figure 5. Temporal evolution of density fluctuations at (a) $\bar{x} = 500$ and (b) $\bar{x} = 1500$. Note the increase in the fluctuation amplitude with decreasing \bar{x} . The inset shows the non-Maxwellian feature of the ion velocity distribution function which is calculated by including all the ions in the region $4000 \leq \bar{x} < 4500$.

Table 2. Ion Beam and Plasma Parameters From Run 2

\bar{t}	\bar{n}_{b1}	\bar{n}_{b2}	V_{b1}	V_{b2}	V_{be}	\bar{T}_{b1}	\bar{T}_{b2}	\bar{T}_e	\bar{C}_e
1000	0.93	0.07	-1.1	0.22	0.32	0.32	0.58	2.6	0.1
1200	0.87	0.13	-0.096	0.19	0.28	0.37	0.74	2.8	0.1
1400	0.82	0.18	-0.086	0.16	0.21	0.42	1.00	3.1	0.12

Another mechanism which contributes to the electron energization deals with the spatial distribution of the slowly time-varying potential as shown in Figure 4g. When the electrons expanding from the plasma sources cross the midpoint of the simulation region, they see an accelerating potential giving rise to an elongated tail of the electron velocity distribution function.

3.3. Consequences of the Ion-Ion Instability

The plasma flow and the potential distribution in the flux tube are significantly affected by the ion-ion instability as seen from Figures 4a to 4r. The instability occurs in the off-central region and in the central region the ion beams continue to counterstream (Figures 4d to 4f). At an early stage, the instability occurs at relatively small scale lengths as seen from the potential distribution in Figure 4i. The subsequent nonlinear evolution of the instability forms vortices, which grow in size as clearly seen from the potential distributions for $\bar{t} \geq 1600$ in Figures 4j, 4k, and 4l. The amplitudes of the potential associated with the vortices are as large as $5 kT_e/e$, which approximately corresponds to the ion beam energy at $\bar{t} = 1400$ when the instability sets in, that is,

$$\frac{1}{2} m_i V_{b2}^2 \cong q \Delta \phi \quad (2)$$

where $\Delta \phi$ is the amplitude of a vortex, q is the charge on an ion, and V_{b2} is the beam velocity of the faster ion beam. The above relationship between V_{b2} and $\Delta \phi$ suggests the possibility of trapping the ions in the vortices. This trapping is evident from Figure 4. The cells with relatively high positive potentials have ions almost completely mixed in velocity space and their velocity spread is reduced in contrast to the relatively large velocity spread in the neighboring negative potential cells. As a matter of fact in the latter cells ions have a "hole" in their velocity distribution function, which is a signature of an ion hole. The electrons' behavior is directly opposite to that of the ions; electrons have large-velocity spreads in the positive potential cells and a relatively small spread in the negative potential cells (see Figures 4p, 4q, and 4r). This alternate trapping of electrons and ions affects the flow of plasma and density distribution in the flux tube. Before we discuss the density distribution and the filling of the flux tube, we point out that another consequence of the ion-ion instability is the formation of electrostatic shocklike structures.

3.4. Electrostatic Shocks

The electrostatic shocklike structures evolve from the ion-ion instability; the vortices having positive potential cells begin to grow in size with increasing time and their edges steepen into shock pairs. The potential distribution plots for $\bar{t} > 1400$ show examples of the formation of some shock pairs as indicated by

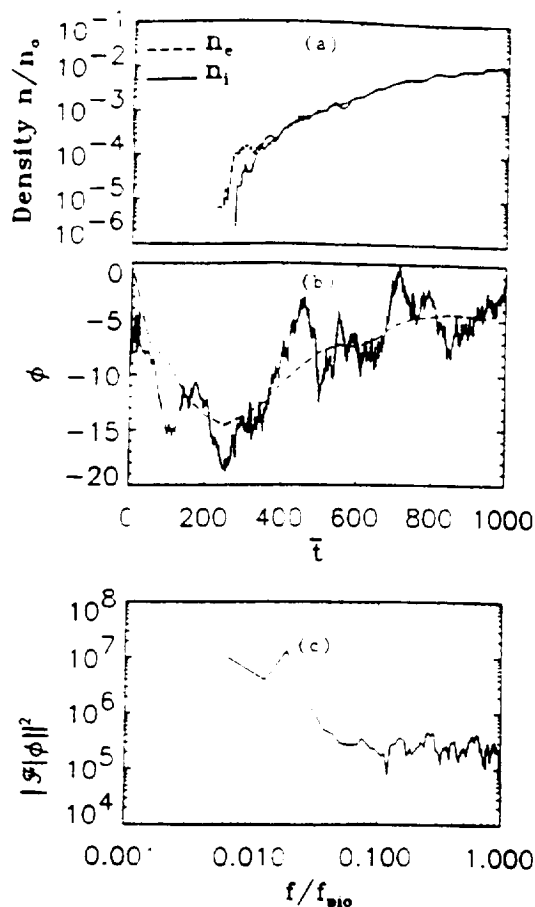


Figure 6. Temporal evolution of (a) Electron and ion densities. (b) Electric potential ϕ , all at $\bar{x} = 2500$. (c) Frequency spectrum of the potential shown in (b). The dotted curve in (b) shows the average potential when the fluctuations are averaged out.

arrows in Figures 4j, 4k, and 4l. Inside a shock pair the potential is positive; ions are mixed and electrons are trapped showing their acceleration above the background electrons [Forstlund and Shonk, 1970a]. The growing size of a positive potential cell is equivalent to the motions of the shocks bounding the cell. This can be seen by comparing the innermost shock pairs on the right-hand side of the center of the simulation region in Figures 4k and 4l. The motion of shocks enables the positive potential cells to merge together. This elevates the potential of the outer region of the flux tube with respect to its ends, as well as with respect to the central region where the potential is negative in a relatively extended region.

We see from Figures 4d to 4f and 4j to 4l that as the innermost shocks bordering the central counterstreaming move inward, the size of the central counterstreaming region decreases. However, this does not continue indefinitely. The evolutions of the ion and electron phase space and that of the potential distribution, for times later than that shown in Figure 4, are given in Figure 7. Figures 7a to 7c for the ion phase space and the corresponding potential distribution in Figures 7g to 7i show that for $\bar{t} \geq 2200$, the central region of ion counterstreaming expands again as the innermost shocks move outward. The corresponding electron phase space plots reveal that in the central negative potential region the electrons'

velocity spread shrinks. Why do the innermost shocks move outward again? The answer to this question lies in the change in the plasma influx into the tube caused by the elevation of the positive potential in its outer regions due to the merging of the positive potential cells as shown in Figures 4k and 4l. The elevated potential chokes the plasma flow into the flux tube. When the ion flux is reduced, the inner shocks begin to move outward to maintain the continuity of the ion flux through the shocks. This phenomenon of shock motion is quite similar to the motion of double layers seen in numerical simulations [Singh and Schunk, 1982] and laboratory experiments [Iizuka et al., 1983]; in these studies it was found that when ion flux to an existing double layer is reduced, the double layer remains stable in its shape, but it moves toward the ion source to keep the ion flux through the double layer at a constant value. The shock and the double layer are both electrostatic structures and it appears that the shock also remains stable in response to the changes in the ion flux by moving in an appropriate direction. For the outward shock motion of the shock in Figures 7g to 7j, the shock velocity is found to be $V_{sh} \approx V_B$ from $\bar{t} = 2200$ to 2800. At later times the i-i instability again inflicts the counterstreaming ion beams as seen from the plots for $\bar{t} > 2800$ in Figure 7. This mixes the ion beams in the outer region of the counterstreaming, but leaving the ions counterstreaming in the central region. It appears that the above process of i-i instability in the outer region, formation of positive potential cells and their merging, shock formations and their motion may repeat a few times before the flux tube fills with a thermalized plasma.

The formation of shocks in the off-equatorial region is predicted by two-stream hydrodynamic models [Rasmussen and Schunk, 1988; Singh, 1990]. But these shocks form due to the slowing down of the ion beams by polarization electric fields and/or Coulomb collisions. A semikinetic model of interhemispheric plasma flow does not show shock formation [Wilson et al., 1992]. Recently Singh et al. [1994] found that in a semikinetic model, which treats electrons by assuming a Boltzmann distribution, the condition for the ion-ion instability in the direction of the plasma flow is not met. Our small-scale simulation discussed here show that the instability conditions can be satisfied by the electron heating due to the electron-ion instability which is driven by relatively fast ion beams and occurs during the early stage of the refilling. When electron dynamics is simplified by assuming the Boltzmann law, this instability is lost along with the associated consequences of electron heating, ion-ion instability, and shock formation.

It is important to point out that dynamics of the shocks seen in two-stream hydrodynamic models is quite different from that seen in run 2. In the former case a shock forms in each stream in the off-equatorial region and subsequently it moves upward to the equator and then downward to the ionospheric boundary. Such shock motions affect the transition from supersonic to subsonic flow for each plasma stream [Singh, 1991a]. The resulting subsonic flows continue to counterstream indefinitely. On the other hand, run 2 shows that the counterstreaming in the off-equatorial region is rather quickly thermalized by the ion-ion instability, and it persists over a longer time only in the central region. However, as seen from Figures 4 and 7 the spatial extent of the central counterstreaming is quite dynamic. Furthermore, we find that the i-i instability should lead to the formation of several shock pairs evolving from the positive potential cells created by the instability [Forstlund and Shonk,

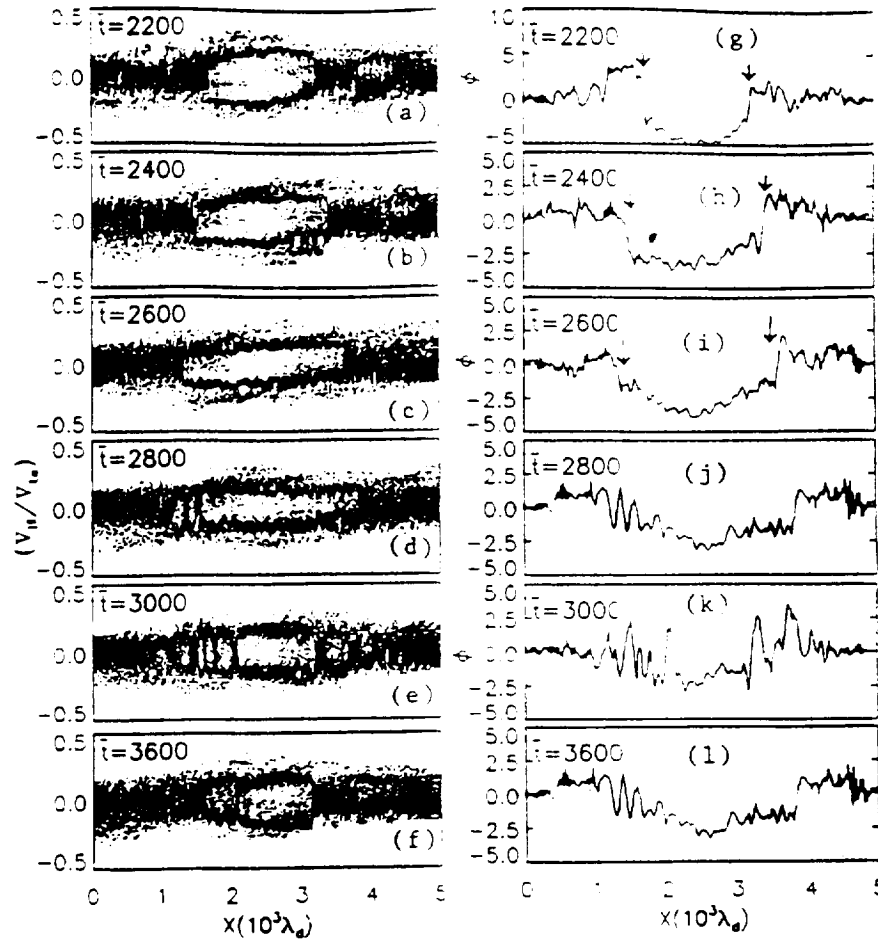


Figure 7. Same as Figure 4, but the plots are for $\bar{t} > 2000$ and the electron phase space is not shown. Note the temporal variation in the spatial extent of the central counterstreaming and the associated charges in the potential distribution.

1970a]. The evolution and merging of such shock pairs has a profound effect on the state of the plasma in the central (equatorial) region.

4. Cold Plasma Flowing Into a Hot Plasma

We discuss here the results from a simulation in which cold plasmas expanding from the plasma reservoirs in Figure 1a come into contact with a hot plasma trapped in the central region of the flux tube where the magnetic field minimizes (Figure 1b). As pointed out earlier, we refer to this simulation as run 3. The situation considered in this simulation corresponds to that of the fast ion streams flowing into the equatorially trapped hot plasma during the early stage of the plasmaspheric refilling. Some preliminary results from this run were presented in a previous paper [Singh, 1993] in which the discussion was limited to shock formation. Here we expand the discussion to other processes affecting the flux tube filling. When the hot plasma is the only plasma in the flux tube, the difference between the temperature anisotropy of electrons and ions sets up electric fields pointing away from the central region, and the corresponding potential distribution is given by [Whipple, 1977]

$$\phi(x) = (kT_e^H/e) [1 + T_{||}^H/T_e]^{-1} \ln(\Gamma) \quad (3)$$

where $\Gamma = (T_{\perp}^H/T_{||}^H)(1 - B_m/B(x)) + B_m/B(x)$, T_{\perp}^H and

$T_{||}^H$ are perpendicular and parallel temperatures of the hot ions, respectively, T_e is the temperature of the warm electrons, B_m is the minimum magnetic field, and $B(x)$ is the magnetic field at the point where the potential is $\phi(x)$.

When $B_m/B \ll 1$ and $T_e \ll T_{||}^H$, (3) is simplified to $\phi(x) \cong (kT_e/e) \ln(T_{\perp}^H/T_{||}^H)$. For $T_e = 10T_o$, and $T_{\perp}^H/T_{||}^H \cong 2$, the potential difference between the point of minimum magnetic field and the point where the magnetic field is $B(x)$ is about $7kT_o/e$. This maximum potential drop is expected without any cold plasma in the flux tube.

Large-scale refilling models [Singh et al., 1986; Wilson et al., 1992] indicate ion flow velocities up to 30 km/s during the early refilling stage, the corresponding kinetic energy of H^+ ion beam is < 5 eV, which is smaller than the maximum potential energy of the ions estimated above for $T_o = 1$ eV. Thus the hot plasma is expected to have a significant effect on the flow of cold plasma, and hence on the refilling processes.

We performed several simulations in which hot plasma properties were varied. We found that as long as hot ions are anisotropic with $T_{\perp}^H > T_{||}^H$ and the warm electrons are isotropic or anisotropic with the reverse anisotropy, that is, $T_{||}^H > T_{\perp}^H$, the basic effects of the hot plasma on the cold plasma flows are the same. Therefore we describe here only the results from the simulation run with the following hot plasma properties: $T_{\perp}^H = 2T_{||}^H = 1800$, and $T_e^H = T_{||}^H = T_e = 10T_o$, where we recall

that T_0 is the cold plasma temperature in the plasma reservoirs in Figure 1a.

Figures 8a to 8l shows the evolution of the ion phase space in the $\bar{x}-\bar{v}_{||}$ plane. Figure 8a for $\bar{t} = 200$ shows the expanding ion beams from the plasma reservoirs at $x=0$ and $x=d$. For showing some details of the cold ion phase space, the vertical scale in Figure 8 is expanded and it does not fully show the velocity space of the hot ions. At $\bar{t} = 400$ (Figure 8b), the ion beams begin to come into contact with the hot plasma. The plot at $\bar{t} = 600$ (Figure 8c) shows that the incoming ion beams are being reflected. This reflection is expected because the potentials set up by the hot plasma provide sufficiently large barriers for the approaching ion beams. The evolution of the potential distribution corresponding to that of the phase space (in Figure 8) is shown in Figures 9a to 9j. An important feature of the potential distribution is the occurrence of a potential pulse coinciding with the central hot plasma for $\bar{t} \leq 1000$. The peak potential at $\bar{t} = 200$ is $15kT_0/e$, which is nearly double the potential predicted by (1). The development of the large potential is attributed to the space charges developing in the system. In contrast, (1) is based on the assumption of a quasi-neutral plasma. The expansion of the cold plasma compresses the potential pulse as seen from the plots in Figure 9 for $200 \leq \bar{t} \leq 800$, after which the edges of the pulse steepen into shock like structures and the pulse broadens again and slowly diminishes in amplitude reaching an asymptotic value of about $5kT_0/e$ at $\bar{t} = 1200$. The broadening of the potential pulse is associated with the outward propagation of the shocks. The evolution of the potential distribution at later times is affected by the shock propagation and, outside the central region between the two shocks, it is also affected by the ion-ion instabilities as

discussed in connection with run 2. The ion-ion instability creates vortices in the $\bar{x}-\bar{v}_{||}$ phase space as seen at $\bar{t} = 1600$ in Figure 8g.

It is useful to discuss the mechanism of the shock formation. When counterstreaming ion beams begin to interpenetrate, a pair of electrostatic shocks form due to the coupling between the ion beams affected by the ion-ion instability [Forslund and Shonk, 1970a; Singh, 1990]. As we discussed in run 2, in the absence of the central hot plasma, the ion beams continue to counterstream indefinitely because their relative beam velocity V_{br} is too fast to satisfy the conditions for the ion-ion instability which are $V_{br} < 2C_s$ and $T_e > 3T_i$ where C_s is the ion acoustic speed and T_e and T_i are the electron and ion temperatures; the instability in the central region does not occur even though the latter condition on temperature is satisfied due to the electron heating by the electron-ion instability. In the present situation with the central hot plasma, the counterstreaming on both sides of the hot plasma is created by the reflection of the ion beams by the central potential barrier. The relative ion beam velocities between the counterstreaming ion beams on both sides of the potential pulse near the reflection point are $V_{br} = 0.5, 0.4, 0.32$, and 0.26 at $\bar{t} = 600, 800, 1000$ and 1200 , respectively. We recall that central hot plasma consists of a warm electron population with temperature $T_e = 10T_0$, which yields an ion acoustic speed $C_s = 0.16$. Thus the condition for the ion-ion instability near the reflection point is satisfied for $\bar{t} \geq 1000$. It is important to point out that the shocks form just outside the region where hot ions are trapped; outside this region the cold ions dominate and satisfy the temperature condition mentioned above. The instability couples and mixes the counterstreaming ion beams forming a "mixed" plasma "tab" developing near the

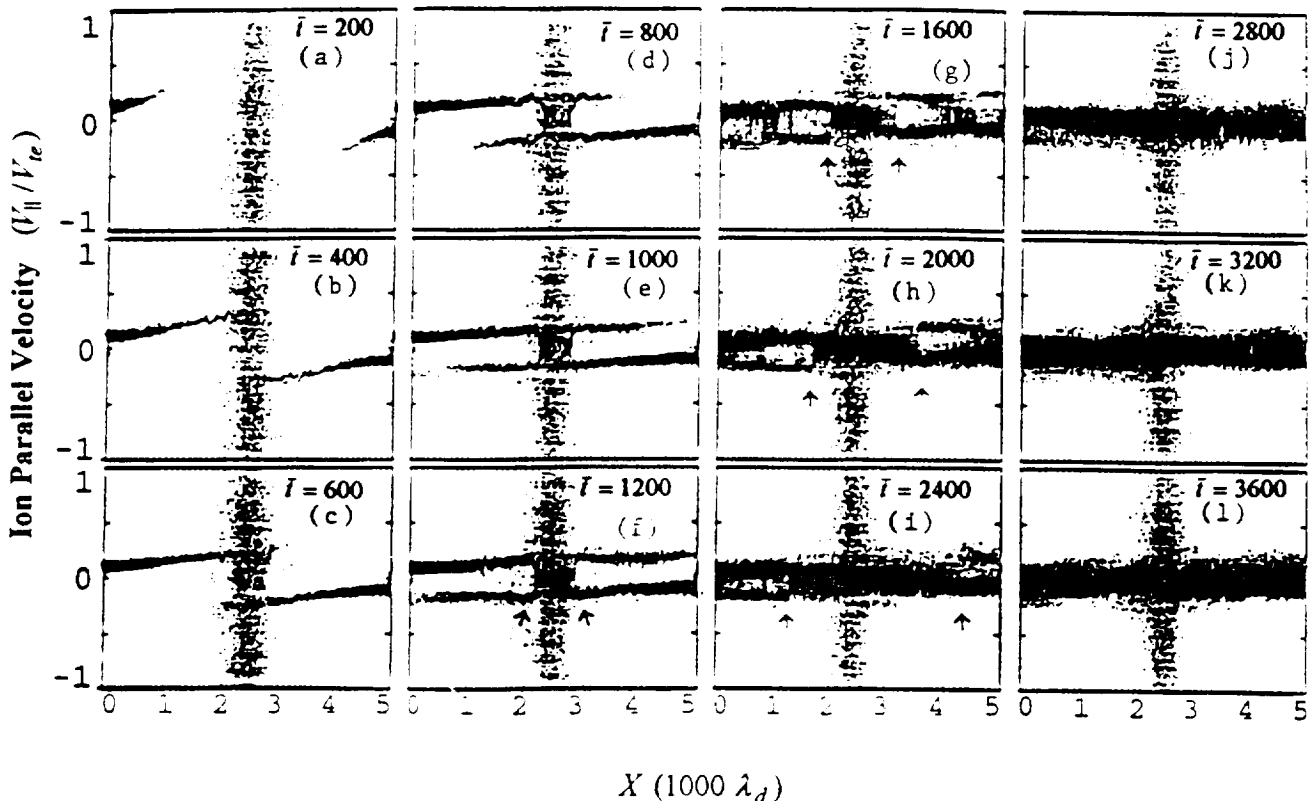


Figure 8. Temporal evolution of ion phase space in the $\bar{x}-\bar{v}_{||}$ plane (run 3). Note the central hot ions; the entire distribution of the hot ions is not shown; it is truncated at $\bar{v}_{||} = \pm 1$ so that the cold plasma distribution can be adequately resolved. Note the reflection of ions, formation and propagation of electrostatic shocks.

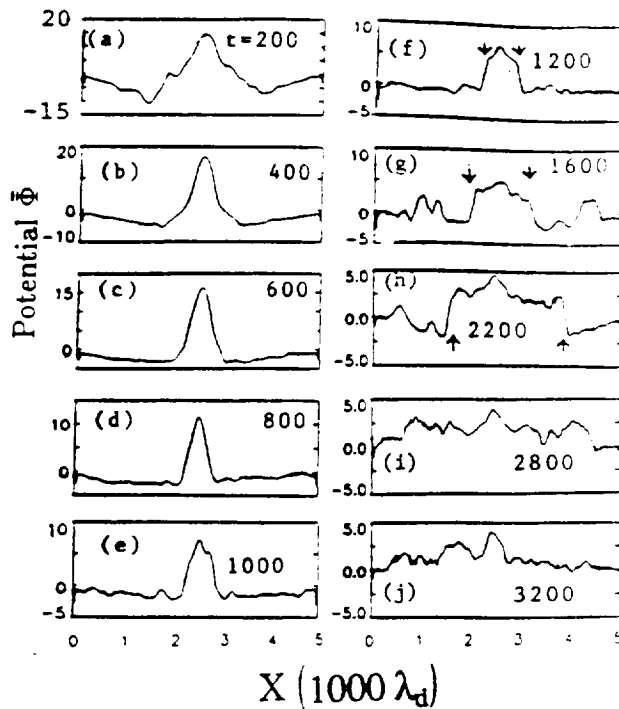


Figure 9. The temporal evolution of the potential distribution corresponding to that of the ion phase space in Figure 8. Note the evolution of the shock from the potential pulse set up by the centrally trapped hot plasma.

shocks, one on each side of the central hot plasma (Figures 8e and 8f); the plasma tabs appear in the phase space plots as the darkest areas between the hot plasma and the counterstreaming ion beams. The extension of the tabs of mixed plasma along with outward propagation of the shocks is clearly seen by comparing the phase space plots in Figure 8 for $\bar{t} = 1200$ and 2400. The outward propagation of the electrostatic shocks are indicated by the arrows in Figures 8f to 8i and Figures 9f to 9i. After their formation at about $\bar{t} = 1200$, shocks move away from the central region with a velocity $V_{sh} \approx 0.05V_{te} \approx V_{te}$, where V_{te} and V_{ti} are the electron and ion thermal speeds in the cold plasma, respectively.

As the shocks propagate out, ion-ion instability occurs in the regions ahead of the shocks as seen at $\bar{t} = 1600, 2000$ and 2400 in Figure 8, the instability creates vortices in the phase space. The combined effects of the shock propagation and the ion-ion instability mix the counterstreaming ion beams nearly all along the flux tube as seen from Figure 8 for $\bar{t} \geq 2800$. This mixing of counterstreaming ion beams all along the flux tube is quite different from what we saw in run 2 that the counterstreaming persists in the central region (see Figures 4a to 4f and 7a to 7f from run 2).

The evolution of the electron phase space, corresponding to those of the ion phase space in Figure 8, and the potential distributions in Figure 9, is shown in Figure 10. The phase space plots shown in this figure are at selected times representing the different stages of the plasma evolution. The prominent features of the electrons before $\bar{t} \leq 400$ are the two spatially separated electron populations: the centrally trapped electrons in the potential well shown in Figure 9 and the electrons expanding into the flux tube from the plasma reservoirs at $x=0$ and $x=d$. For $\bar{t} \geq 1200$, we see the signature of the shock pair in the electron phase space; the

centrally trapped electrons develop sharp edges like the potential distribution (Figure 9) and the ion phase space (Figure 8), all marked by arrows. Along with the outward propagating shocks, the centrally trapped electrons expand away from the central region. Even after the shocks have propagated out to the boundaries, the electron phase space shows a gradual "bulging" from the ends to the central region, in agreement with the potential distribution in Figure 9 for $\bar{t} \geq 2400$ when the potential in the central region remains positive and the potential distribution has gentle gradients giving electric fields pointing toward the ends.

Figure 8 for $\bar{t} \leq 800$ shows that as the cold plasmas expand to the central hot plasma, ion beams are reflected, while the cold electron gas is accelerated toward the center by the parallel electric fields given by the central potential pulse. Therefore, in the early stage the cold ion beams are initially excluded from the central region, but eventually the electrons pull them into the hot plasma region. When the cold electrons are accelerated by the central potential pulse, the additional negative charge lowers the peak potential after $\bar{t} > 600$ as seen from Figure 9. This allows the cold ions to penetrate into the hot plasma region. The penetration is clearly seen from the ion phase plots in the $\bar{x}-\bar{v}_\perp$ plane as shown in Figure 11. As seen from Figure 8, at times prior to $\bar{t} = 400$ the hot ions trapped in the central region are separated from the cold ions in

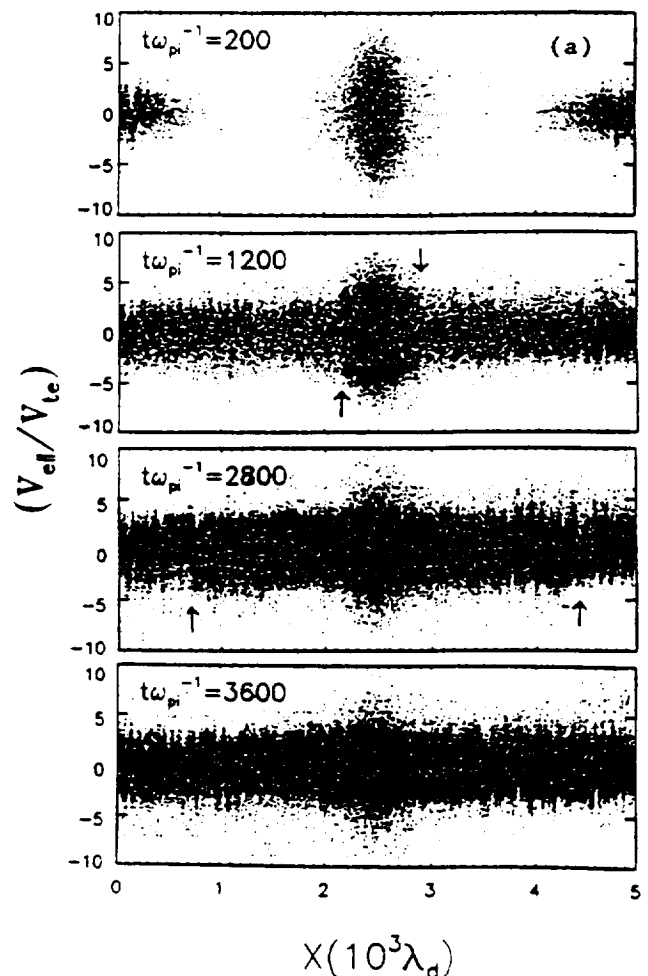


Figure 10. The temporal evolution of the electron phase space in $\bar{x}-\bar{v}_\perp$ plane corresponding to that of the ions in Figure 8 and the potential distribution in Figure 9.

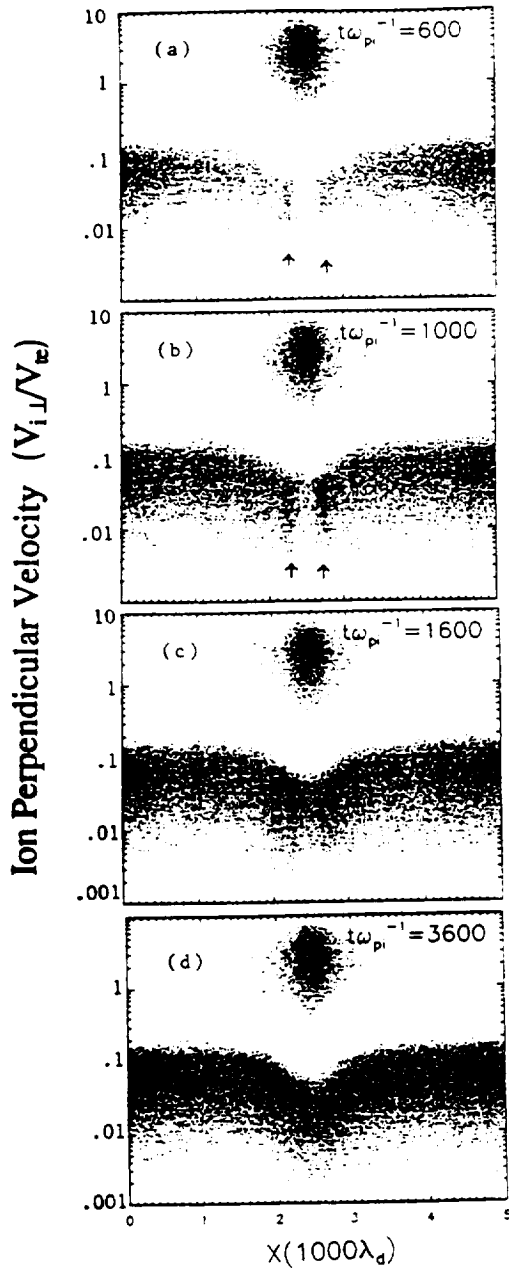


Figure 11. Evolution of ion phase space in the $\bar{x}-\bar{v}_\perp$ plane (run 3). Note the presence of the centrally trapped hot ions. At early times the expanding cold ions create density fronts when they come into contact with the hot plasma as shown by arrows. The fronts eventually punch through the hot plasma mixing the cold and hot plasmas spatially.

the configuration space. Figure 11a shows the situation when the cold ion beams come into contact with the centrally trapped hot plasma, having perpendicular velocities up to about $\bar{v}_\perp = 9$. As the cold plasmas expand and the ions reflect from the potential barrier, there are accumulations of plasmas near the reflection points forming fronts which move toward the midpoint of the simulation region as seen from the plots for $600 \leq \bar{t} \leq 1600$ in Figure 11. By the time $\bar{t} = 1600$, the cold ions have punched through the potential barrier, and the further evolution of the $\bar{x}-\bar{v}_\perp$ phase space does not reveal any new feature. The $\bar{x}-\bar{v}_\perp$ phase space plot at the end of the

simulation run is shown in Figure 11d. Later we discuss the perpendicular velocity distribution function of the ions consisting of the cold and hot populations as seen from this figure. The evolution of the electron phase space in $\bar{x}-\bar{v}_\perp$ does not reveal any noteworthy feature, except that, like the ions, electrons have a warm population trapped in the central region along with the cold electrons.

Evolution of the plasma density distribution in the flux tube is shown in Figure 12. The density distribution at $\bar{t} = 200$ shows that the cold plasma is well separated from the centrally trapped hot plasma. The maximum normalized density of the hot plasma is about 0.05. As the cold plasmas expand, eventually the density maximum at the midplane ($\bar{x} = 2500$) disappears and a density minimum occurs there. In our simulation, this occurs at about $\bar{t} = 800$. In a recent paper Olsen *et al.* [1994] suggested that the equatorial density distribution of the trapped ions with $T_\perp > T_\parallel$ depends on the electron temperature anisotropy; specifically they suggested that for isotropic electrons the trapped ion density distribution has a density maximum at the equator. On the other hand, when $T_{e\parallel} > T_{e\perp}$ the density distribution has minimum at the equator. Our simulation shows that the occurrence of the density maximum or minimum depends on the stage of the mixing of the cold and the hot plasmas. When the hot plasma density dominates, the trapped ion density profile has a density maximum where the magnetic field minimizes. When the cold plasma flow begins to dominate the hot plasma density, the maximum disappears and a density minimum appears in its place.

The shocks seen in the ion phase space (Figure 8) and the potential distribution (Figure 9) are also seen from the density distributions for $\bar{t} = 2000$ in Figure 12; the shocks are indicated by the arrows. Figure 12 shows the filling of the flux tube with the cold plasma flowing into it from the plasma reservoirs. Later we discuss the filling in more detail.

4.1. Plasma Distribution Functions

The hot-cold plasma interaction produces some interesting features in the velocity distribution functions of the ions in the flux tube. We briefly describe these features here. We examine the distribution functions from two regions of the flux tube; near the ends of the tube, say for $100 \leq \bar{x} \leq 500$, and in the central region $2300 \leq \bar{x} \leq 2700$. The evolution of the ion distribution functions near the ends of the tube is shown in Figure 13. At early time, as shown for $\bar{t} = 200$, the distribution shows an ion beam flowing into the flux tube. Eventually, precipitating ions appear as an ion beam for $V_\parallel < 0$; for example, as shown for $\bar{t} = 1200$. As time elapses, the ion beams for $V_\parallel < 0$ and $V_\parallel > 0$ merge together. The above evolution of the ion distribution function is the combined effect of the expansion of the cold plasma into the flux tube, loss of some of the hot ions injected into the magnetic trap, reflection of the expanding ion beams from the electrostatic shocks (see Figure 2) and the ion-ion instability. A noteworthy feature of Figure 13 is that the precipitating ($V_\parallel < 0$) ions have energies greater than the inflowing ions. This merely reflects that some of the precipitating ions have undergone acceleration by the potential distribution set up by the hot plasma. In the course of the simulation, the midpoint ($\bar{x} = 2500$) potential varies from about $18kT_o/e$ to $5kT_o/e$ (Figure 9). Thus the precipitating ions cover a spectrum of energy extending to about $15kT_o/e$ which corresponds to a maximum velocity of about $0.3V_{te}$ as

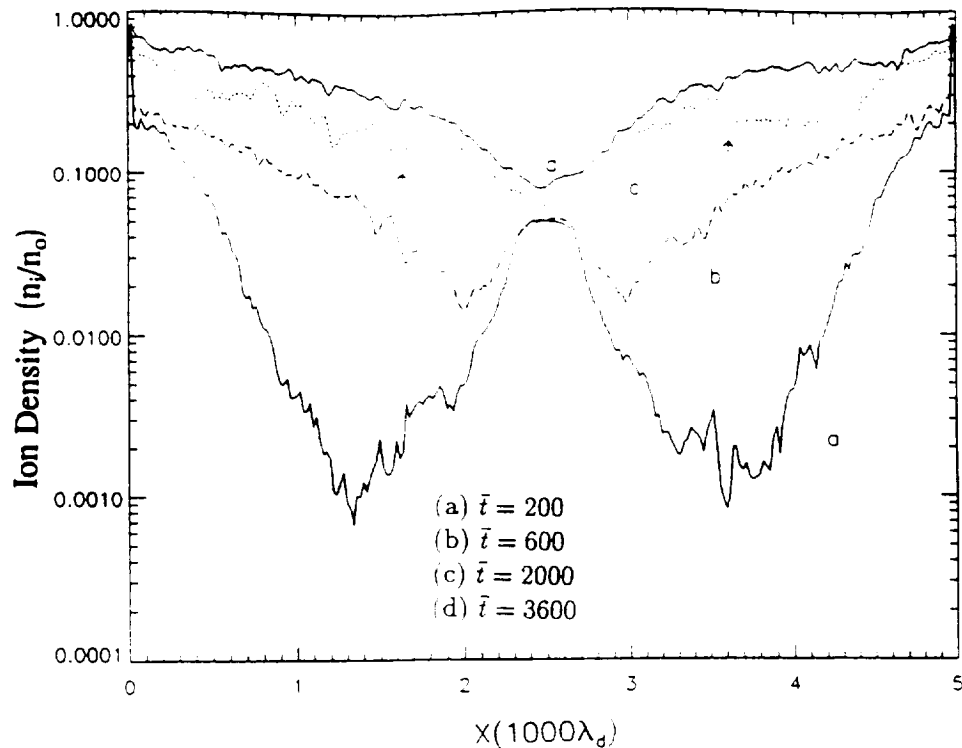


Figure 12. Temporal evolution of the total ion density in the flux tube (run 3). At early times the hot plasma creates a density maximum at the center. As the cold plasma fills the tube, the density maximum eventually disappears. The signature of the electrostatic shocks in the density distribution is indicated by the arrows on the density profile for $\bar{t} = 2000$.

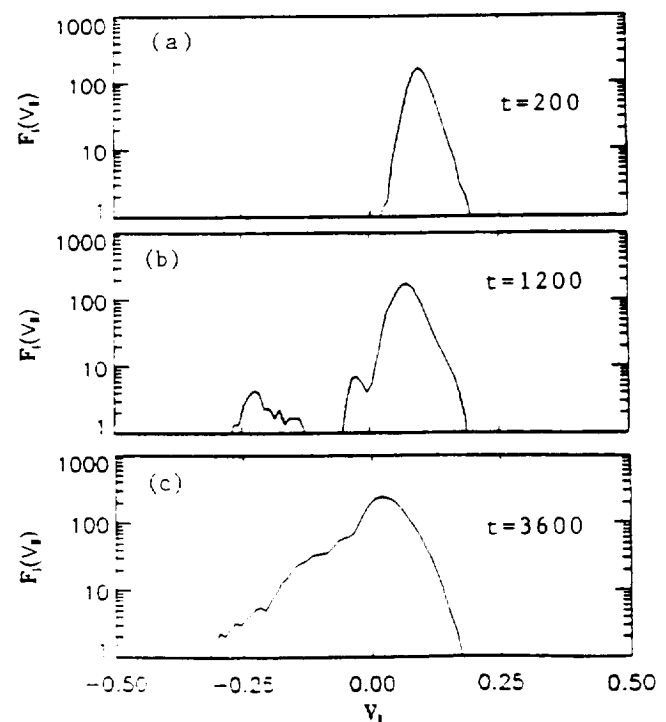
seen in Figure 13 for $V_{\parallel} < 0$. The shape of the distribution function in Figure 13c suggests a heatflow from the central region toward the ends of the flux tube.

The mixing of the hot and cold plasmas in the central region produces distribution functions having a core of cold ions and a halo of hot ions. Such parallel and perpendicular velocity distribution functions are shown in Figures 14a and 14b, respectively. (These distribution functions are for the ions in the central region ($2300 \leq \bar{x} \leq 2700$)). In the parallel velocity distribution the cold core and the relatively hot ion populations are merged, but in the perpendicular velocity distribution, the hot ions are well separated from the cold population and they extend from a low velocity of $\bar{V}_{\perp} = 0.2$ to large velocities corresponding to that of the injected hot plasma. As we shortly show, the hollow between the cold and hot ion population is simply the consequence of the loss of the hot ions from the magnetic trap in the presence of parallel electric fields. The hot ion population in Figure 14b appears as a beam in V_{\perp} . Since in gyrophase these hot ions are randomly distributed, the beam is a ring distribution in the perpendicular velocity. The ring distributions of energetic ions with energies 5–30 keV have been observed in the equatorial region of the outer plasmasphere and they are known to excite fast magnetosonic waves [Perraut *et al.*, 1982].

However, the ring distribution seen from the simulation is considerably less energetic in the sense that its low energy end begins at an energy determined by the peak potential of the positive potential pulse seen in the simulations (Figure 9).

The hollow between the cold and hot ion populations in the perpendicular velocity distribution (Figure 14b) is caused by the

Figure 13. Evolution of the ion velocity distribution function $F_{\parallel}(V_{\parallel})$ near the end of the flux tube ($100 \leq \bar{x} \leq 500$, run 3). Note the ions reflected ($V_{\parallel} < 0$) from the central potential pulse created by the initial hot plasma. Eventually the inflowing and the reflected ions merge together. Asymmetry of the distribution function suggests heat flux from the central region toward the end of the flux tube.



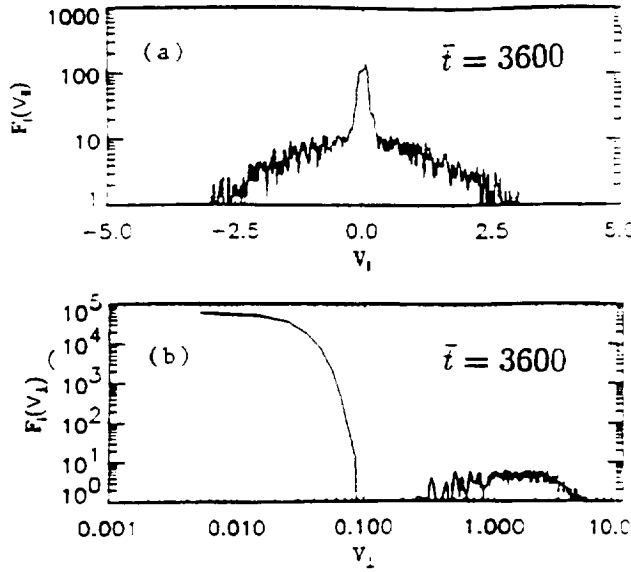


Figure 14. Ion velocity distribution functions at $\bar{t} = 3600$ in the central region of the flux tube where hot and cold ions have spatially mixed (run 3). (a) $F_i(V_{||})$ and (b) $F_i(V_{\perp})$. Note the presence of the cold core ions and the hot ions appearing as a halo in $F_i(V_{||})$ and a beam in $F_i(V_{\perp})$.

potential created by the hot plasma. Some of the ions from the hot ion population, having sufficiently low perpendicular velocities, are accelerated into the loss cone by the electric field set up by the centrally peaked potential distribution (Figure 9) and precipitate out of the flux tube. The minimum perpendicular velocity ($V_{\perp \text{min}}$), below which the ions precipitate out, can be estimated by the conservation of energy and the magnetic moment. A simple calculation shows that the hot ions trapped in the central region must satisfy the following relation between their parallel ($V_{||0}$) and perpendicular ($V_{\perp0}$) velocity components [Whipple, 1977],

$$V_{\perp0}^2 \geq [V_{||0}^2 + (\frac{2q\phi_0}{m_i})] (B/B_{\text{min}} - 1)^{-1} \quad (4)$$

where ϕ_0 is the maximum potential at the center of the flux tube with respect to the ends where the magnetic field is B . B_{min} is the magnetic field at the center. When $\phi_0 = 0$, (4) gives the usual loss cone in a magnetic mirror with the mirror ratio $R = B/B_{\text{min}}$. For nonzero ϕ_0 , the loss cone is appreciably modified near $V_{||0} \sim 0$. The minimum perpendicular velocity above which hot ions are trapped occurs for $V_{||0} = 0$, and it is given by

$$V_{\perp \text{min}} = (2q\phi_0/m_i)^{1/2} / R^{1/2} \quad (5)$$

For the parameter of our simulation $V_{\perp \text{min}} \approx 0.1 V_{1e}$, which turns out to be smaller than the value seen from the simulation (Figure 14b), and is attributed to the fluctuations in ϕ_0 .

Although the ions from the hot population are lost for $V_{\perp} < V_{\perp \text{min}}$, the region near $V_{\perp} \sim 0$ is populated by the cold ions as the cold plasma flows punch through the potential barrier (Figure 11). Thus the resulting distribution as shown in Figure 13b is potentially unstable. The modified loss cone has the feature of a ring distribution for driving waves due to its positive

slope ($\partial f / \partial V_{\perp} > 0$) near $V_{\perp} \approx V_{\perp \text{min}}$. In context of the equatorial plasma, we have identified here a new source of free energy for exciting waves resulting from the hot-cold plasma interpenetration [Singh *et al.*, 1993]. Since $V_{\perp \text{min}} \ll V_A$, the Alfvén velocity, we expect an excitation of relatively slow waves capable of heating cold ions. The heating has the potential of generating superthermal ions bridging the gap between the cold and the hot ion populations and thereby producing a continuum of energy distribution from about ~ 1 eV to the characteristic energies of the hot ions.

5. Flux Tube Filling

After examining the evolutions of the plasma in the three simulations, we examine now the flux tube filling. We compare here the plasma distributions and the flux tube contents as seen from the three runs. Figures 15a and 15b show the comparison of the ion density distributions from run 1 and run 2 at $\bar{t} = 2000$ and 3600, respectively. Figure 15a shows that compared to run 1, in run 2 the filling is depressed in the central region, while it is enhanced in the off-central region at $\bar{t} = 2000$. The explanation for this feature of the filling lies in the potential distribution as shown in Figures 4j to 4l. The elevated potentials in the off-central region inhibit the flow of plasma into the central region; this keeps the ion density depressed there and therefore the plasma entering the flux tube accumulates in the outer regions of the flux tube. We find that until about $\bar{t} = 2000$ the net plasma contents of the flux tube in run 1 and run 2 are approximately the same. This is seen by curves 1 and 2 in Figure 16, in which the total number of computer ions accumulated in the flux tube is plotted as a function of time for the two runs.

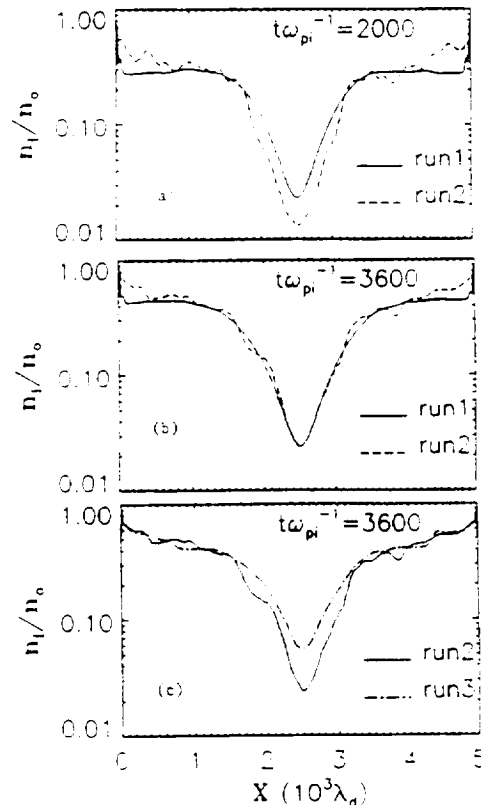


Figure 15. Comparison of the density distributions in the flux tube from different simulations. Run 1 and run 2 at (a) $\bar{t} = 2000$ and (b) $\bar{t} = 3600$. (c) Run 2 and run 3 at $\bar{t} = 3600$.

Figure 15b shows that eventually the ion densities in the central region of the flux tube in the two runs become nearly equal. This is due to the fact that the potential barriers for the ions in the outer region of the flux tube reduces as seen by comparing the potential distributions in Figures 4j, 4k, and 4l for $\bar{t} < 2000$ with those in Figures 7g to 7l for $\bar{t} > 2000$. However, the densities in the off-central region in run 2 remains generally larger than that in run 1. This yields a larger plasma content in the former run than that in the latter. Curves 1 and 2 in Figure 16 clearly show this for $\bar{t} > 2000$. The enhanced refilling in run 2 is attributed to the trapping of ions and electrons in the vortices set up by the ion-ion instability.

Figures 15a, 15b and curves 1 and 2 in Figure 16 show that the plasma waves enhance the filling of the flux tube by trapping plasma in vortices set up by the ion-ion instability. We find that the hot plasma injected into the central region of the flux tube has a similar effect on filling with the cold plasma, although through additional processes. In order to demonstrate this, we compare the filling of the flux tube as seen from run 2 and run 3. Curves 2' and 3 in Figure 16 show the comparison of the flux tube contents from run 2 and run 3. Curve 2' is the same as curve 2, but it is translated along the vertical axis by the initial number of the hot ions injected into the flux tube at $t = 0$ in run 3. Curve 3 shows the evolution of the plasma content from run 3. The vertical translation of curve 2' is done for the purpose of easy comparison of the cold plasma contents of the flux tube as seen from these runs. A comparison of curve 2' with curve 3 shows that the initially injected hot plasma facilitates the trapping of more cold plasma than that from the run without the hot plasma. In the simulation with the initially injected hot plasma (run 3) enhanced trapping occurs by two processes: (1) the vortices set up by the ion-ion instability enhance the filling like the enhanced filling in run 2 over that in run 1; (2) the potential pulse and its evolution in an extended

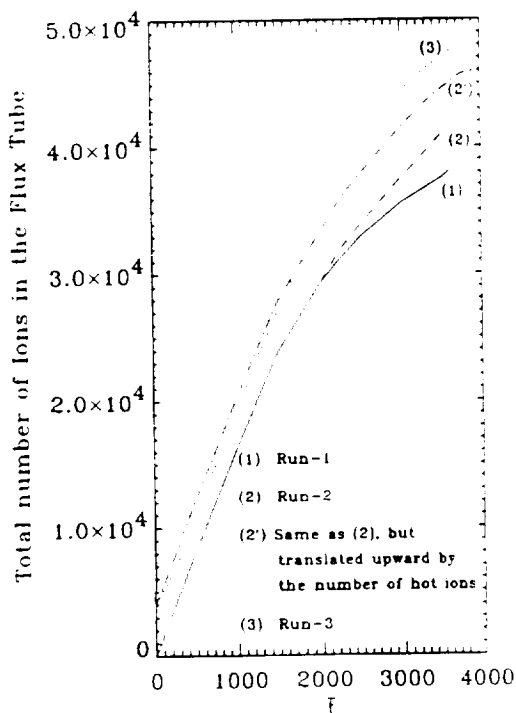


Figure 16. Comparison of the flux tube contents from run 1 and run 2, and run 2 and run 3. Note the enhanced filling in run 2 over run 1 and in run 3 over run 2.

potential distribution (Figure 9) provide an additional mechanism for the trapping of the cold plasma. When the cold plasma flows into the flux tube, the electric fields set up by the extended potential distribution slowly retard the flow and increase the ion density in the flux tube. The effect of this additional mechanism on the enhanced filling is illustrated in Figure 15c, in which we compare the density profiles at the end of the simulations in run 2 and run 3. We notice that the enhanced density is confined in the central region from $\bar{x} \approx 10^3$ to 4×10^3 . One can argue that this enhanced density is due to the centrally trapped hot plasma, but the comparison of the total plasma contents from run 2 and run 3 in Figure 16 clearly points out that the cold plasma content is enhanced. Since Figure 15c shows that the relative density enhancement in run 3 occurs over an extended region only inside the central portion of the flux tube, it is obvious that an additional amount of cold plasma is also contained in that region. The containment of the additional cold plasma is facilitated by the retardation of the inflowing ions by the relatively weak electric fields associated with the extended potential distribution in Figure 9 for $\bar{t} > 2400$.

6. Conclusions and Discussion

By means of numerical simulations, we have studied here anomalous plasma effects on the accumulation of plasma in a magnetic flux tube. The anomalous effects are caused by ion-beam-driven instabilities and by the interaction between a cold plasma flowing into the magnetically trapped hot plasma. The main conclusions from the simulations on the ion-beam-driven instabilities and its effect on filling of the flux tube are the following:

1. As the magnetic flux tube fills with a plasma expanding from plasma sources located at its end, the ion-beam-driven instabilities significantly affect (1) the distribution and dynamics of the plasma in the tube and (2) the accumulation of plasma in it.
2. Two types of instabilities are found to occur: the instability caused by electron-ion interaction is kinetic in nature and occurs when the ion beams are relatively fast, and electron dynamics is not simplified by the assumption of the Boltzmann law. The ion-ion instability occurs for comparatively slower ion beams.
3. In the simulation with the Boltzmann electron, the electron-ion instability is suppressed and the ion beams remain too fast with respect to the ion acoustic speed to excite ion-ion waves. However, as the beams slow down by the filling of the flux tube, they tend toward the marginal instability, especially in the outer region of the flux tube, where the plasma fluctuation is enhanced. This causes an anomalous scattering of the beam ions in the outer region.
4. In simulation with the kinetic treatment of the electrons, e-i instability occurs when the beams are relatively fast and it heats the electrons. In addition, some electron energization occurs when they are accelerated by the inward pointing electric fields set up by the counterstreaming plasma expansion. When electrons are sufficiently heated, increasing the ion acoustic speed so that $V_{be} \leq 2C_s$, the ion-ion instability occurs.

5. The ion-ion instability is effective in coupling the counterstreaming ion beams in the region where instability conditions are met. This sets up potential structures including electrostatic shocks. The central counterstreaming is seen to spatially shrink and expand as the ion-ion instability and its nonlinear features affecting the plasma evolve.

6. The trapping of plasma in the potential structures enhances the flux tube refilling and affects the distribution of the plasma in it.

7. In the central region of the flux tube where the magnetic field is minimum, the fast ion beams continue to counterstream over a relatively long time.

Following the work of Banks *et al.* [1971], now there are several studies on shock formation including large-scale hydrodynamic [Singh *et al.*, 1986; Guiter and Gombosi, 1991; Rasmussen and Schunk, 1988] and kinetic models [Wilson *et al.*, 1992; Singh *et al.*, 1994] and small-scale simulations [Singh *et al.*, 1986; Singh, 1988]. The usual picture emerging from such studies is the formation of a pair of shocks in the equatorial region or in the off-equatorial region, one in each hemisphere. The simulation presented here suggests that when i-i instability occurs, it may create numerous shock pairs in the off-equatorial region. Their merging and dynamics may introduce both spatial structures in the plasma distribution and temporal features in the evolution of the plasma state, both in the equatorial and off-equatorial regions.

It is important to point out that in the present study based on one-dimensional simulations, oblique i-i acoustic and ion-cyclotron modes are excluded. These modes become especially relevant when the ion beams become too fast ($V_b > C_s$) to excite the magnetic-field aligned parallel propagating i-i acoustic modes [Forslund and Shonk, 1970b; Karimabadi *et al.*, 1991]. When the beams are sufficiently fast and the plasma temperatures are not favorable for the acoustic modes, the beams may drive ion cyclotron waves [Foote and Kulsrud, 1981]. The relative roles of parallel and oblique acoustic modes, and of ion cyclotron waves in thermalizing the ion beams during the different stages of the filling of a magnetic flux tube remain to be studied.

The main conclusions from the simulation with the equatorially trapped hot plasma are as follows:

1. Hot plasma creates a potential barrier for the cold plasma flow. The magnitude of the potential differs from that given by theory [Whipple, 1977] which does not account for the presence of the cold plasma. We show that the potential evolves as the hot and cold plasmas interact [Singh, 1993].

2. The main feature of the evolution of the potential distribution is the formation and propagation of the electrostatic shocks. We saw in run 2 that in the absence of the hot plasma, the counterstreaming expansion of cold plasma in the flux tube sets up counterstreaming ion beams, which last for a relatively long time in the central region. In contrast to this, the potential barrier set up by the hot plasma reflects the incoming plasma flow on each side of the centrally trapped hot plasma. In the early stage the cold plasmas do not penetrate into the central region of the hot plasma. The reflection of ion beams sets up counterstreaming on each side of the hot plasma. The shock formation begins in the reflection region where beams are relatively slow and the warm electrons give a relatively large ion acoustic speed. These two effects create the conditions for the ion-ion instability (see run 2), and hence the shocks form.

3. The propagation of the shock extends the positive potentials created by the hot plasma to large distances from where the hot plasma is trapped.

4. As the shocks propagate away from the central region of the flux tube, ion-ion instability occurs in the outer regions, as described in run 2. The combined effects of the shocks and the

vortexes set up by the instability create an extended potential distribution, in which central region of the flux tube remains generally positive.

5. The extended potential distributions help in trapping more cold plasma than that in the run without the hot plasma. The trapping occurs by retarding the inflowing ions in the flux tube. Thus the filling of the flux tube with the cold plasma is enhanced by the presence of the equatorially trapped hot plasma.

6. The plasma distribution functions resulting from the hot-cold plasma interaction show some interesting features. We found that the precipitating ion beams and electrons, which are leaving the simulation system, are energized by the plasma processes occurring in the flux tube. This suggests that the hot-cold plasma interaction may eventually deposit some energy into the topside ionosphere during the refilling of a plasmaspheric flux tube.

7. The ion velocity distribution function in the central region consists of a cold core and a halo of hot ions. In the perpendicular velocity distribution, the hot ions appear as a ring starting at a low perpendicular energy which approximately corresponds to the maximum potential barrier set up by the hot plasma population. Such ring distributions can generate waves in the frequency band from the ion gyrofrequency to the lower hybrid frequency [Lee and Birdsall, 1979]. However, such waves cannot be studied by the one-dimensional simulations used in the present work.

In view of the findings of this paper regarding the anomalous effects of ion-beam-driven instabilities, a pertinent question is whether they are relevant to the refilling of plasmaspheric flux tube. Since the ion beams are inherent to the early stage refilling, the answer to this question is solidly yes. In view of the crudeness in the temporal and spatial resolution of the large-scale refilling models, the most pertinent question is how to include the effects of the instability in such models. At this juncture the answer to this question is not very clear, but we know that it must be done by calculating anomalous plasma transport coefficients which can be included in the large-scale treatments. The heating of electrons and ions by the instability can be included through an anomalous collision frequency like that for ion-cyclotron instability in the auroral plasma [Ganguli and Palmadesso, 1987], but how to include the effect of ion and electron trapping in potential structures set up by the ion-ion instability remains a challenge. Even though the simulations presented here show that the anomalous effects enhance the flux tube refilling, a quantitative estimate of the enhancement in the refilling of an outer plasmaspheric flux tube must await the inclusion of the anomalous effects in the large-scale models.

The simulation with the centrally trapped hot plasma showed that despite the potential barrier set up by the plasma, the cold ion beams do penetrate into the hot plasma region. This spatial mixing generates unstable plasma velocity distributions (Figure 14b) which can drive waves, eventually mixing the hot and cold plasmas in velocity space as well.

Acknowledgments. This work was supported by NASA grant NAGW-2128 made to the University of Alabama in Huntsville. The Editor thanks D. Winske and another referee for their assistance in evaluating this paper.

References

- Banks, P. M., A. F. Nagy, and W. I. Axford, Dynamical behavior of thermal protons in the mid-latitude ionosphere and magnetosphere, *Planet. Space Sci.*, 19, 1053, 1971.

- Baker, D. R., Nonlinear development of the two ion beam instability, *Phys. Fluids*, **16**, 1730, 1973.
- Deforest, S. E., and C. E. Mcllwain, Plasma clouds in the magnetosphere, *J. Geophys. Res.*, **76**, 3587, 1971.
- Foote, E. A., and R. M. Kulsrud, Stability of colliding ion beams, *Phys. Fluids*, **24**, 1532, 1981.
- Forslund, D. W., and C. R. Shonk, Formation of electrostatic collisionless shocks, *Phys. Rev. Lett.*, **25**, 1699, 1970a.
- Forslund, D. W., and C. R. Shonk, Numerical simulation of electrostatic counterstreaming instabilities in ion beams, *Phys. Rev. Lett.*, **25**, 281, 1970b.
- Fried, B. D., and A. Y. Wong, Stability limits for longitudinal waves in ion-beam-plasma interactions, *Phys. Fluids*, **9**, 1084, 1966.
- Fujita, T., T. Ohnuma and S. Adachi, Self-oscillations excited by two stream ion-ion instability, *Plasma Phys.*, **19**, 875, 1977.
- Ganguli, S. B., and P. J. Palmadesso, Plasma transport in the auroral return current region, *J. Geophys. Res.*, **92**, 8673, 1987.
- Gresillon, D., and F. Doveil, Normal modes in the ion-beam-plasma system, *Phys. Rev. Lett.*, **34**, 77, 1975.
- Guiter, S. M., and T. I. Gombosi, The role of high-speed plasma flows in plasmaspheric refilling, *J. Geophys. Res.*, **95**, 10,427, 1990.
- Hasegawa, A., *Plasma Instabilities and Nonlinear Effects*, chap. 2, Springer-Verlag, New York, 1975.
- Ichimaru, S., *Basics of Plasma Physics*, chap. 11, Benjamin-Cummings, Reading, Mass., 1973.
- Iizuka, S., P. Michelsen, J. J. Rasmussen, R. Schritwieser, R. Hatakeyama, K. Saeki, and N. Sato, Double layer dynamics in a collisionless magnetoplasma, *Rep. Riso -M-2414*, Riso National Laboratory, Riso, Denmark, 1983.
- Karimabadi, H., N. Omidi, and K. B. Quest, Two dimensional simulations of the ion-ion acoustic instability and electrostatic shocks, *Geophys. Res. Lett.*, **18**, 1813, 1991.
- Khazanov, G. V., M. A. Kuen, Y. V. Konikov, and I. M. Sidorov, Simulation of ionosphere-plasmasphere coupling taking into account ion inertia and temperature anisotropy, *Planet. Space Sci.*, **32**, 585, 1984.
- Lee, J. K. and C. K. Birdsall, Velocity space ring plasma instability, magnetized, part 1: Theory, *Phys. Fluids*, **22**, 1306, 1979.
- Lin, J., J. L. Horwitz, G. R. Wilson, C. W. Ho, and D. G. Brown, A semikinetic model for early stage refilling: 2. Effects of wave-particle interactions, *J. Geophys. Res.*, **97**, 1121, 1992.
- McKee, C. F., Simulation of counterstreaming plasmas with application to collisionless electrostatic shocks, *Phys. Rev. Lett.*, **18**, 990, 1970.
- Olsen, R. C., C. R. Chappell, D. L. Gallagher, J. L. Green, C. R. Campbell, and R. R. Anderson, Plasma observations at the magnetic equator, *J. Geophys. Res.*, **92**, 2385, 1987.
- Olsen, R. C., L. J. Scott, and S. A. Boardsen, Comparison between Liouville's theorem and observed latitudinal distributions of trapped ions in the plasmasphere region, *J. Geophys. Res.*, **99**, 2191, 1994.
- Perraut, S., A. Roux, P. Robert, R. Gendrin, J.-A. Sauvaud, J.-M. Bosqued, G. Kremser, and A. Korth, A systematic study of ULF waves above F_H^+ from GEOS-1 and -2 measurements and near relationship with proton ring distributions, *J. Geophys. Res.*, **87**, 6219, 1982.
- Rasmussen, C. E., and R. W. Schunk, Multistream hydrodynamic modeling of interhemispheric plasma flow, *J. Geophys. Res.*, **93**, 14,557, 1988.
- Roux, A., S. Perraut, J. L. Rauch, C. De Villedary, G. Kremser, A. Korth, and D. T. Young, Wave particle interactions near Ω_{H^+} observed on board GEOS 1 and 2, 2. Generation of ion cyclotron waves and heating of H^+e ions, *J. Geophys. Res.*, **87**, 8174, 1982.
- Singh, N., Ion-Electron instability of ion-beam-plasma systems, *Phys. Lett. A*, **67**, 372, 1978.
- Singh, N., Refilling of a plasmaspheric flux tube: Microscopic plasma processes, in *Modeling Magnetospheric Plasma*, *Geophys. Monogr. Ser.*, vol. 44, edited by T. E. Moore and H. H. Waite, p. 87, AGU, Washington, D.C., 1988.
- Singh, N., Comment on "Multistream hydrodynamic modeling of interhemispheric plasma flow, by C. E. Rasmussen and R. W. Schunk, *J. Geophys. Res.*, **95**, 17, 272, 1990.
- Singh, N., Role of ion temperature anisotropy in multistage refilling of the outer plasmasphere, *Geophys. Res. Lett.*, **18**, 817-820, 1991a.
- Singh, N., Role of electromagnetic noise in the interhemispheric plasma exchange along closed field lines, *Adv. Space Res.*, **11** (9), 51-54, 1991b.
- Singh, N., Interaction of field-aligned cold plasma flows with an equatorially-trapped hot plasma: Electrostatic shock formation, *Geophys. Res. Lett.*, **20**, 799, 1993.
- Singh, N., and C. B. Chan, Effects of equatorially trapped ions on refilling of the plasmasphere, *J. Geophys. Res.*, **97**, 1167, 1992.
- Singh, N., and K.S. Hwang, Perpendicular ion heating effects on the refilling of the outer plasmasphere, *J. Geophys. Res.*, **92**, 13,513, 1987.
- Singh, N., W. J. Raitt, and F. Yasuhara, Low energy ion distribution functions on a magnetically quiet day at geostationary altitude ($L=7$), *J. Geophys. Res.*, **87**, 681, 1982.
- Singh, N., and R. W. Schunk, Dynamical features of moving double layers, *J. Geophys. Res.*, **87**, 3561, 1982.
- Singh, N., and R. W. Schunk, Numerical simulations of counterstreaming plasmas and their relevance to interhemispheric flow, *J. Geophys. Res.*, **88**, 7867, 1983.
- Singh, N., R. W. Schunk, and H. Thiemann, Temporal features of the refilling of a plasmaspheric flux tube, *J. Geophys. Res.*, **91**, 13,433, 1986.
- Singh, N., and D. G. Torr, Effects of ion temperature anisotropy on the interhemispheric plasma transport during plasmaspheric refilling, *Geophys. Res. Lett.*, **17**, 925, 1990.
- Singh, N., G. R. Wilson, J. L. Horwitz, Comparison of hydrodynamic and semikinetic treatments for a plasma flow along closed field lines, *J. Geophys. Res.*, **99**, 11,495, 1994.
- Whipple, E. C., The signature of parallel electric fields in a collisionless plasma, *J. Geophys. Res.*, **82**, 1525, 1977.
- Wilson, G. R., J. L. Horwitz, and J. Lin, A semikinetic model for early stage plasmasphere refilling, 1, Effects of Coulomb collisions, *J. Geophys. Res.*, **97**, 1189, 1992.

W. C. Leung and N. Singh, Department of Electrical and Computer Engineering, University of Alabama, Huntsville, AL 35899.

(Received May 4, 1994; revised September 16, 1994; accepted October 26, 1994.)

**Effects of Electrostatic Ion Cyclotron
Wave Instability on Plasma Flow
During Early Stage Plasmaspheric Refilling**

Nagendra Singh

Department of Electrical and Computer Engineering
University of Alabama in Huntsville
Huntsville, AL 35899

Submitted to JGR October 1995

Abstract

Mesoscale models for the plasmasphere refilling reveal that the expansion of the ionospheric plasma into empty flux tubes during the early stage refilling produces highly supersonic counterstreaming ion beams. Such beams are found to meet the conditions for the instability of the electrostatic ion cyclotron (eic) waves in the equatorial plasmasphere. Since the spatial scale of the eic wave instability is determined by the ion Larmor radius and the corresponding time scale by the ion cyclotron period, it is unresolvable by the crude spatial and temporal resolutions afforded by the mesoscale models. Thus the eic waves and the associated microprocesses are missed out by the existing mesoscale refilling models based on the fluid and semikinetic approaches. We propose here an algorithm for incorporating the effects of eic waves on mesoscale plasma flow; the algorithm is based on the critical conditions for the eic instability. When the relative drift of the counterstreaming ion beams exceeds a critical value, depending on the beam temperatures, the excess momentum and energy are dissipated into thermal motion of the ions, resulting in ion heating in the degree of freedom perpendicular to the ambient magnetic field at the expense of the parallel ion drift. This leads to the creation of two distinct ion populations consisting of field-aligned counterstreaming ions and perpendicularly heated warm anisotropic ions trapped in the flux tube. The latter ions are created during the first few hours of the refilling process primarily in the equatorial region, but eventually they spread out all over the flux tube. Highly anisotropic ions are seen near the equator by the virtue of being locally created and trapped there. Estimates of the Coulomb collision time show that the warm anisotropic population (WAP) has a life time ranging from about 10 hours in the topside ionosphere to several days in the equatorial region. Thus, once initially created during early stage refilling, WAP ions become a common feature of the outer plasmasphere. The coexisting multiple ion populations, consisting of anisotropic warm ions and the field-aligned counterstreaming flows, have been observed from DE 1 on flux tubes undergoing refilling.

1. Introduction

Since the early work of *Banks et al* [1970], models have shown that highly supersonic counterstreaming ion beams occur in the equatorial region during the early stage plasmaspheric refilling after geomagnetic storms. This has been demonstrated further by both hydrodynamic and semikinetic models [*Singh et al*, 1986; *Rasmussen and Schunk*, 1988; *Singh*, 1991; *Wilson et al*, 1992]. Following the work by *Banks et al* [1970], *Schulz and Koons* [1971] suggested that the electrostatic ion cyclotron (eic) waves driven by the beams might be scattering the ions in pitch angle, trapping them in the flux tube, and thereby contributing to the refilling process. Since the self-consistent treatment of the eic wave excitation and the heating of ions by wave-particle interactions in a mesoscale refilling model is a difficult task, the early suggestion of *Schulz and Koons* [1972] did not get incorporated in the subsequent refilling models. The small-scale simulations motivated by the refilling problem have been primarily limited to the parallel ion-acoustic waves driven by the ion-ion interaction leading to the formation of electrostatic shocks [*Singh and Schunk*, 1983; *Singh et al*, 1986; *Singh and Leung*, 1995]. The purpose of this paper is to demonstrate that the eic wave instability driven by counterstreaming ion beams is distinctly possible during early stage plasmaspheric refilling, and that when the effects of the waves are properly included in a mesoscale model, the resulting ion populations consist of field-aligned counterstreaming and warm anisotropic ions having remarkable similarities with those observed from the DE 1 satellite [*Sojka et al*, 1983].

One of the fascinating observations from DE 1 is the simultaneous observation of thermal ion populations having quite different energy and pitch angle distributions [*Sojka et al*, 1983]. Such multiple ion populations are not limited to the equatorial region as discussed by *Olsen et al* [1987] and *Lin et al* [1995], but they extend to quite high geomagnetic latitudes on flux tubes from $L \cong 3$ to 8. As summarized by *Sojka et al* [1983], these populations are as follows: (1) a thermal plasma (TP) population, which is isotropic and has a temperature between 1.5 and 3 eV. This population is the main constituent of the outer plasmasphere; (2) a warm anisotropic plasma (WAP) population with pitch angle distribution having a maximum at 90° and temperature

ranging from 5 to 20 eV ; and (3) a thermal field-aligned (TFA) population consisting of counterstreaming beams in the vicinity of the plasmopause, and beyond it the observed beams are from the closest ionosphere only. With increasing L beyond the plasmopause region, the TP population is progressively replaced by the TFA ions. So far the mechanisms for the creation of this multi-population thermal plasma in the refilling region remain nearly unexplored. The inclusion of the effects of eic waves during the early stage refilling reveals a possible mechanism for generating the different coexisting ion populations. The eic waves also create a relatively energetic ion population having perpendicular energies up to several tens of eV with a high degree of thermal anisotropy as reported by *Olsen* [1981] and *Olsen et al* [1987]. These highly anisotropic ions are tightly confined to the equatorial region, and they are created during the very early stage of the onset of interpenetrating ion beams in the equatorial region.

Since the generation of waves by ion beams and subsequent wave-particle interactions are micro-scale processes, they are generally missed out due to the relatively large spatial grid sizes and time steps used in the mesoscale models. In this paper we describe a procedure to include the effects of microprocesses driven by the ion beams on the evolution of the mesoscale plasma flow during refilling. The basic paradigm behind our procedure is that the waves are driven when the ion beams exceed the critical conditions on the relative beam velocity and temperatures. When the mesoscale processes drive the beams away from the critical conditions toward instabilities, the driven waves tend to restore the plasma to the critical conditions. This idea is similar to that of Gary et al [1994] to determine the hot proton anisotropy by the critical condition for the proton cyclotron instability in the magnetosphere. In the next section, we examine the instabilities driven by ion-beam plasma systems. We show that during the early stage of the interpenetration of the ionospheric ion beams, eic waves are the most likely waves to be driven. We describe the procedure to implement the effects of this wave on the mesoscale plasma flow. Other possible waves are not considered in this implementation for the sake of simplicity and also due to the lack of a clear understanding about their effects on the mesoscale flow.

The rest of the paper is organized as follows. In section 2 we give a brief review of the relevant instabilities, and we examine here whether or not the instability conditions are met during the early stage refilling. Section 3 deals with the recipe for including the effects of eic waves in a mesoscale model. Numerical results from the model are presented in section 4. Conclusions of the paper are discussed in section 5.

2. Plasma Instabilities in Counterstreaming Ion Beams

It will be useful to briefly review the waves and instabilities which occur in counterstreaming ion beams before we apply them to a mesoscale model. In a plasma with counterstreaming ion beams the waves are driven by electron-ion (e-i) and ion-ion (i-i) interactions [e.g., see *McKee, 1972; Fujita et al. 1977; Singh, 1978*]. The acoustic waves driven by the e-i interaction leads to electron heating [*Davidson, 1972; Singh and Leung, 1995*]. On the other hand, the major effect of the waves driven by i-i interactions is the modification in the ion flow [*McKee, 1970*].

Depending on the parameters of the plasma, the i-i interaction is likely to drive two wave modes, which are the i-i acoustic waves and the electrostatic ion-cyclotron (eic) waves [*Foote and Kulsrud, 1981*]. For symmetric counterstreaming ion beams with beam velocities $\pm V_b$, ion thermal velocity $V_{tb} = (k_B T_i / m_i)^{1/2}$, and nondrifting background electrons with a temperature T_e , a summary of the marginal stability condition is as follows. Note that k_B is the Boltzmann constant, T_i is the ion temperature, and m_i is its mass. Figure 1 shows the marginal stability condition in the $(T_i / T_e) - (V_b / V_{tb})$ plane. For $V_b / V_{tb} < 1.3$, the system is stable for all values of T_i / T_e . When $1.3 \leq V_b / V_{tb} \leq 2.1$, the i-i acoustic waves propagating parallel to the beam velocity ($V_b \parallel \underline{B}$) are dominant and $(T_i / T_e)_c$ increases with increasing (V_b / V_{tb}) . For $2.1 \leq V_b / V_{tb} \leq 4.2$, the oblique i-i acoustic waves propagating at an angle $\theta = \cos^{-1}(2.1 V_{tb} / V_b)$ are dominant and the $(T_i / T_e)_c$ remains constant at ~ 0.3 . When $V_b / V_{tb} > 4.2$, the eic waves dominate and the critical temperature rises with increasing V_b .

Let us now examine if the above instability conditions are met during the early stage of refilling. For this purpose we used a mesoscale refilling model based on a semikinetik code in which ions are treated kinetically while electrons are assumed to be a massless fluid with a constant temperature [*Wilson et al, 1992; Singh et al, 1994*]. The latter assumption yields that the electrons obey the Boltzmann law. The geometry of the flux tube undergoing refilling is shown in Figure 2. We model a flux tube covering geomagnetic latitudes from $\lambda = \lambda_o$ in the northern hemisphere to $\lambda = -\lambda_o$ in the southern hemisphere. We measure distances along the

magnetic field line from $S = 0$ at $\lambda = \lambda_o$, and it increases with decreasing λ . The magnetic field in the flux tube varies with λ according to the dipolar field.

Figure 3 shows the evolution of the outflow of plasma from the conjugate ionospheres into an initially empty flux tube without any wave-particle interactions. This figure shows the phase space plot of the flow of H^+ ions in the $S - V_{\parallel}$ plane. We have considered the refilling of an initially empty flux tube with $L = 4$, and the ionospheric boundaries at $\lambda_o = 57.5^\circ$ with the corresponding altitude of the boundaries at 1000 km. The main feature of the ionospheric outflow is that counterstreaming of ions begins in the equatorial region at about $t = 15$ minutes, and it progressively spreads all over the flux tube. In order to examine the instability criteria, bulk properties of the individual ion beams are calculated. Figure 4 shows the properties of the flow coming out from the northern hemisphere ($\lambda > 0$) at $t = 30$ minutes. Figure 4a shows the latitudinal distribution of the average flow velocity normalized to the ion thermal velocity in the ionosphere given by $V_{th} = (k_B T_o / m_i)^{1/2}$, where m_i is the H^+ mass and T_o is the ionospheric plasma temperature. Note that the electron and ion temperatures in the ionosphere are assumed to be the same, that is $T_i = T_e = T_o$. Figure 4b shows the evolution of the ion beam temperature (T / T_o) as a function of λ for the beam originating from the northern ionosphere. Figures 4a and 4b also hold good for the flow coming out of the southern hemisphere by replacing λ with $-\lambda$. Since the instability requirements involve V_b normalized to the local beam thermal velocity V_{tb} , we have plotted the normalized velocity $V_b / V_{t\ell}$ in Figure 4c, where local thermal velocity $V_{t\ell}(\lambda) = (k_B T / m_i)^{1/2} = V_{tb}$. The use of $V_{t\ell}$ emphasizes that the V_{tb} varies with the geomagnetic latitude according to the beam temperature T in Figure 4b. We note from Figure 4b that the beam temperature in the equatorial region decreases to a value as low as $\leq 0.2 T_o$, which yields an electron to ion temperature ratio $T_i / T_e \cong 0.2$. Such low beam temperatures may be conducive to the i-i acoustic instability, but the beams are too fast for this mode to dominate [Foote and Kulsrud, 1981]. We note from Figure 4c that $V_b / V_{t\ell} \sim 10$ in the equatorial region. We also point out that during the early time interval from $t = 15$ to $t = 30$ minutes, the normalized beam velocity can be as large as $V_b / V_{t\ell} \sim 30$ in the equatorial region where the beams interpenetrate.

The horizontal broken line in Figure 4c shows the minimum critical ion beam velocity above which the eic instability occurs. In view of Figures 1 and 4c, we find that the fast ion beams can easily drive the eic mode in the equatorial region, and at the same time they are too fast for the i-i acoustic mode to dominate. In this paper we limit ourselves to examine the effect of the eic waves on the refilling plasma. The major effect of this wave is perpendicular ion heating because $E_{\perp} \gg E_{\parallel}$ where E_{\perp} and E_{\parallel} are the wave electric field components perpendicular and parallel to the ambient magnetic field, respectively. We do not include here the subsequent phase of oblique i-i acoustic waves when the ion beams slow down to the critical condition for the eic instability. A major reason for limiting this study to eic waves is that at present we do not rigorously understand how the energy in excess of that given by the critical instability conditions for the oblique i-i acoustic waves is partitioned in parallel and perpendicular heating of ions. For this purpose a separate study based on multidimensional small-scale particle simulation is needed to quantify the partition of the energy before the wave effects are rigorously included in a mesoscale model. The previous simulation study on oblique acoustic waves driven by ion beams by *Forslund and Shonk* [1970] does not include an ambient magnetic field, which has important effects when the transition from the eic to i-i oblique acoustic wave instability occurs.

3. Recipe for Anomalous Plasma Effects

During the early stage of the refilling, the ions are continually accelerated by the large-scale process of plasma expansion [Singh and Schunk, 1983], while the instabilities tend to slow and thermalize them. Thus, the problem of plasma instability during the refilling process is *not* an initial value problem; it is a continually driven system. However, the driving force in the form of a pressure difference between the ionosphere and the equator diminishes as the flux tube refills. If the instability(ies) is (are) fast enough, the plasma flow is kept near the marginally stable conditions. The time step (Δt) used in advancing solutions in large-scale models is generally so large (several seconds) that the instabilities are sufficiently fast to keep the plasma near the marginal stability at the time scale of $\sim \Delta t$. *In this sense, the asymptotic state of the plasma from the instability standpoint is known in advance*; it is the marginally stable state for the dominant instability. Therefore, a recipe for including the anomalous plasma effects in large-scale models can be devised as follows. When the macroscopic forces drive the plasma away from the marginal stability toward an instability, we know exactly the amount of momentum that has to be lost from the counterstreaming flows, and also the amount of kinetic drift energy that is available to be converted into thermal energy through the instability process. Of course, the degree of freedom into which the thermal energy goes, i.e., into heating parallel and/or perpendicular to the ambient magnetic field, depends on the instabilities. For the eic waves which dominate for $V_b > 4.2 V_{tb}$, perpendicular ion heating is of primary importance. A recipe for including the effects of eic waves in the form of perpendicular ion heating in a mesoscale plasma flow is as follows.

If the flow velocity is $V_b(x, t)$ at a given location x and time t , the momentum loss by the instability process on a per particle basis is given by

$$\Delta M = m_i (V_b(x, t) - V_{crit}) \quad V_b(x, t) > V_{crit}$$

where V_{crit} is the velocity above which an instability occurs. If we allow this momentum loss to occur over the entire time step Δt used in a large-scale model, the rate of momentum change due to the waves is

$$\left(\frac{\delta M}{\delta t}\right)_w = \begin{cases} -\frac{m_i}{\Delta t}(V_b(x,t) - V_{crit}) & , \quad V_b(x,t) \geq V_{crit} \\ 0 & , \quad V_b(x,t) < V_{crit} \end{cases} \quad (1)$$

The corresponding heating rate is given by

$$\left(\frac{\delta T_{\perp}}{\delta t}\right)_w = \begin{cases} \frac{1}{2k_B} \frac{m_i}{\Delta t}(V_b^2(x,t) - V_{crit}^2) & , \quad V_b > V_{crit} \\ 0 & , \quad V_b < V_{crit} \end{cases} \quad (2)$$

where T_{\perp} is the perpendicular ion temperature. The above expressions for the momentum and energy change are easily adaptable in mesoscale models based on plasma transport equations [Singh, 1991] and also in semikinetik models based on a PIC code [Wilson *et al*, 1992].

The recipe for the anomalous effects given above is similar to that used by Ganguli and Palmadesso [1987] for the current driven instability in the auroral plasma. It is worth mentioning again that the momentum and energy change implied by equations (1) and (2) may occur at a much faster rate over a time $\tau_w \ll \Delta t$. However, the time constant τ_w determined by the wave process is not known and it is difficult to estimate it. Fortunately, its knowledge is not essential for the calculations; the momentum and energy changes can be spread over the time step of the mesoscale model, as implied by equations (1) and (2), without impacting the mesoscale behavior. The above procedure for including anomalous plasma effects in the mesoscale model based on the critical conditions for the eic instability is conceptually similar to that used by Gary *et al* [1994] to determine the hot proton anisotropy by the marginal condition for the proton cyclotron instability in different regions of the magnetosphere.

We have implemented the above scheme in a semikinetik PIC code [Wilson *et al*, 1992; Singh *et al*, 1994]. The implementation is done as follows. First we check for the occurrence of counterstreaming ion beams. Once counterstreaming occurs we check for the instability conditions. The instability conditions for the eic waves is graphically given by the linear portion of the curve for $V_b > 4.2 V_{ib}$ in Figure 1. This graphical result is implemented by approximating it by the following analytical expression:

$$(T_i / T_e)_c \cong 0.3 + 0.13 (V_b / V_{tb} - 4.2) \quad (3)$$

where $(T_i / T_e)_c$ denotes the critical electron to ion temperature ratio for the eic instability

If the instability conditions are met, the momentum and energy in excess of the critical beam velocity are dissipated. The excess momentum is lost by slowing down ions in a random fashion and the excess energy is dissipated by invoking a perpendicular heating for the ions. The heating is also implemented in a random fashion as described by *Brown et al* [1991]. Whether an ion receives perpendicular energy depends on the probability density function given by

$$p(\Delta w_{\perp}) = \frac{1}{2\pi\sigma} \exp[-1/2(\Delta w / \sigma)^2] \quad (4)$$

where Δw_{\perp} is the impulse of energy given to a H^+ macroparticle in the degree of freedom perpendicular to the magnetic field. In implementing this scheme, a random number R_n is chosen from a uniform distribution from 0 to 1 for each H^+ macroparticle in spatial region where the plasma conditions exceed the instability. This number is compared against the cumulative probability associated with the above probability density and when the latter exceeds R_n , the energy of the particle is increased by Δw_{\perp} . *Brown et al* [1991] showed that the above scheme gives a heating rate given by

$$\frac{\partial k_B T_i}{\partial t} = \sigma / 1.14 \Delta t \quad (5)$$

where Δt is the time step used in advancing the motion of the H^+ macroparticle. Equation (5) in combination with equation (2) defines the heating parameter σ used in (4).

4. Numerical Results

The effects of the eic wave heating on the evolution of the plasma in the flux tube ($L = 4$) is shown in Figure 5. Like in Figure 3, the left hand panel of Figure 5 shows the phase space plots in the $S - V_{\parallel}$ plane. The right-hand panel of Figure 5 shows the evolution of the ions in the $S - V_{\perp}$ plane. The ion beams coming from the opposite directions begin to interpenetrate at the equator at about $t \sim 0.25$ hour. When the counterstreaming ion beams exceed the marginal condition for the generation of eic waves as given by equation (3) derived from Figure 1, we invoke ion heating perpendicular to the ambient magnetic field. The phase space plots at $t = 30$ minutes show the effects of this heating. The heated ions first appear near the equator and they progressively spread all over the flux tube. In terms of the parallel velocity distribution, the heated ions occupy nearly the entire velocity range between the counterstreaming ion beams. This feature of the parallel velocity distribution is the consequence of the following two factors. One is that on the average the relative drift velocity between the counterstreaming ion beams decreases as the perpendicular heating occurs. A check on the energy conservation shows that the total energy, consisting of the parallel and perpendicular energies, before and after the implementation of the perpendicular heating remains the same. This simply implies that the gain in perpendicular energy is at the expense of the parallel energy. The other factor for the spread in the parallel velocity distribution is that when the perpendicularly heated ions move into the opposite hemisphere, they progressively slow down by the mirror force. Ions having large perpendicular energies mirror close to the equator and tend to fill the velocity region near $V_{\parallel} \cong 0$, while those having progressively smaller perpendicular energies travel farther towards the ionospheric boundaries. Some of these ions are lost from the ends of the flux tube while others mirror back. Thus even though the heating occurs primarily in the equatorial region where the eic instability conditions are easily met, the perpendicularly heated ions spread all over the flux tube producing a warm anisotropic population.

The total number of heated ions trapped in the flux tube saturates in about 4 hours, implying the cessation of the loss of the heated ions through the ends of the flux tube. The

heating terminates even earlier at $\tilde{t} \sim 1$ hour when the average beam velocity reaches the critical velocity depending on the local temperature of the ion beams. After the trapping of the heated ions in the flux tube, the plasma in the flux tube evolves ever so slowly.

The phase space plots for $t > 1$ hour in Figure 5 show that there are two distinct plasma populations all over the flux tube. One is the counterstreaming field-aligned flowing ions, which are quite cold in the perpendicular degree of freedom. The perpendicular velocities of such ions evolves adiabatically. In the $S-V_{\perp}$ plots these ions appear as a dark thin band near $V_{\perp} \sim 0$. These field-aligned flowing ions are analogous to the TFA population observed by *Sojka et al* [1983]. The other population, as already mentioned, consists of the warm anisotropic ions. Such ions extend all along the flux tube and they are analogous to the WAP population reported by *Sojka et al* [1983]. The anisotropic ions having the largest perpendicular energies occur near the equator, where maximum perpendicular velocity $V_{\perp \max} \sim 20 V_{tH}$ giving a maximum perpendicular energy $W_{\perp \max} \cong 200 kT_o$. If we assume $T_o = 0.3 eV$, the heated ions are expected to have energies $\leq 60 eV$. These equatorially trapped ions appear as a spatial peak near $\lambda \cong 0$ in the $S-V_{\perp}$ phase space for $t > 2$ hours in Figure 5. However, the number of such ions is quite small compared to that in the field-aligned flow. We note that the warm ions having such relatively large perpendicular energies are created at the expense of the parallel energies of the field-aligned ions, which are the forerunners in the expanding ionospheric plasma in the initially empty flux tube, and have relatively large parallel energies during the very early stage of the refilling at times from 15 to 30 minutes. The equatorially trapped ions with relatively large energies are analogous to the anisotropic ion population reported by *Olsen* [1981] and *Olsen et al* [1987].

The distribution functions of the ions in the equatorial region are shown in Figures 6a and 6b. The perpendicular velocity distribution $F(V_{\perp})$ shows a cold core and a warm ion population as discussed above. The parallel distribution in Figure 6a shows the field-aligned beams, but the velocity space between the beams appear to be filled. The average beam velocity turns out to be about $\pm 4 V_{tH}$. This usual format of presenting the distribution function is somewhat misleading

in showing the real nature of the ion beams. In order to reveal the parallel velocity distribution functions of the beams clearly, we have plotted in Figure 7a the distribution of ions in the $V_{\parallel} - V_{\perp}$ plane. We see from this figure that there are two distinct ion populations and the counterstreaming ion beams remain distinctly separate, unlike the merging shown in Figure 6a. Figure 7 also shows the WAP population. The appearance of merging in Figure 6a is caused by the warm ions having low parallel velocities including $V_{\parallel} \cong 0$. As seen from Figure 7a, the warm ions have the largest perpendicular velocities when $V_{\parallel} \sim 0$. These ions are found to be trapped in the equatorial region appearing as a spatially peaked distribution near $\lambda = 0$ in the $S - V_{\perp}$ phase space in Figure 5 for $t > 2$ hours. At earlier times the equatorially peaked distribution is not so clear because heated ions are still in the process of being lost. After this process is completed, loss cones clearly appear as seen from Figure 7a. In view of their small parallel and relatively large perpendicular velocities, these equatorially trapped ions are highly anisotropic and appear as the trapped ions observed from SCATHA and DE 1 satellites [Olsen, 1981; Olsen *et al*, 1987].

Our simulation shows that the warm anisotropic ions are not necessarily confined to the equatorial region as seen from Figures 7b and 7c which show the ions in the $V_{\parallel} - V_{\perp}$ plane in the off-equatorial regions. However, those confined in the equatorial region show the strongest anisotropy as emphasized by Olsen *et al* [1987]. We also see from Figure 7a that regions near $V_{\parallel} \sim 0$ and $V_{\perp} \sim 0$ are virtually unpopulated. Since the gyrophase can be uniformly distributed between 0 and 2π , the actual distribution of the WAP population is a toroid, but somewhat extended along V_{\parallel} and distinctly having a loss cone. Ring distributions observed by satellites are a special case of the toroid.

The features of the ion distributions in the $V_{\parallel} - V_{\perp}$ plane in the off-equatorial regions shown in Figures 7b and 7c reveal that the counterstreaming ion beams progressively tend to merge as the geomagnetic latitude λ increases, and that the WAP ions have relatively less perpendicular energies (velocities) compared to that in the equatorial region.

The results presented above are for a flux tube with $L = 4$. We found an identical evolution of plasma for a flux tube with $L = 6$, except for some delay when the ion beams

originating from the conjugate ionospheres begin to interpenetrate. This is merely associated with the transit time of the beams from the topside ionosphere to the equator.

Flux Tube Refilling: The accumulation of plasma in the flux tube including the eic wave heating is shown in Figure 8. It is seen that the refilling saturates by the time $t \sim 4$ hours, when the equatorial density has built up to $n \cong 4 \times 10^{-2} n_o$. It has been shown previously by *Wilson et al* [1992] that in the absence of any heating and collisional effects the refilling saturates in a few hours essentially determined by the transit time of the ions from one end of the flux tube to the other. The inclusion of the eic wave heating also leads to a saturation in the refilling in a few hours depending on the transit of the heated ions from the equatorial region to the ends of the flux tube. For the flux tube with $L = 4$, the saturation occurred in about 4 hours. However, we find that the heating and consequent trapping of ions in the flux tube leads to significantly higher densities mostly in the equatorial region of the flux tube. The comparison between the density profiles for the cases with and without the eic waves is shown in Figure 9 for $t = 4$ hours. Without the heating the saturated equatorial density is $1.6 \times 10^{-2} n_o$, and with the heating it is increased to about $4 \times 10^{-2} n_o$. If we assume $n_o \cong 10^3 \text{ cm}^{-3}$, these densities translate to 16 cm^{-3} to 40 cm^{-3} for the cases with and without the eic wave heating, respectively.

In the present paper we have not included collisional effects as previously done by *Wilson et al* [1992]. The ion-ion Coulomb collisions are found to trap the field-aligned flowing ions in the flux tube, keeping the density continually increasing until the refilling saturates in about a day. The effects of collisions on the refilling including the eic wave effects will be addressed later in a separate paper. However, we do discuss here some expected consequences of ion-ion Coulomb collisions. The collisions are much more effective when ion densities are higher and the ion energies are smaller. For a H^+ plasma, the ion-ion collision frequency $\nu \cong 8 \times 10^{-7} n W^{-3/2} \text{ s}^{-1}$ where n is the plasma density in cm^{-3} and W is the total ion energy in eV . For the WAP ions, a typical energy is 10 eV and assuming that $n \cong 100 \text{ cm}^{-3}$ near the ionospheric ends of the flux tube, we have $\nu = 2.5 \times 10^{-6} \text{ s}^{-1}$ and the collision time $\tau = 1/\nu = 11$ hours. If we had chosen $W = 20 \text{ eV}$, keeping the density the same, $\tau = 20$ hours. This implies that the WAP ions once

generated can last nearly up to about one day in the off-equatorial region. In the equatorial region where densities are lower and energies are higher, the life time of the WAP ions increases. For example, if we chose the equatorial density 40 cm^{-3} (Figure 8) and the maximum energy seen in the simulation which is 60 eV , the life time of the equatorially trapped ions is more than 10 days. This simply implies that once created during the early stage refilling, trapped ions become nearly a permanent feature of the equatorial region, unless they are convected away during the geomagnetic storms which deplete the outer plasmasphere. If the flux tube refills from bottom to top by the Coulomb collisions as suggested by *Wilson et al* [1992], the increase in density should isotropize the WAP ions at the time scale of the refilling at high latitudes, but the equatorially trapped ions must persist much longer because of the relatively low equatorial density.

5. Conclusion and Discussion

The main aim of this paper is to incorporate the effects of ion beam-driven waves on the mesoscale evolution of plasma in a refilling outer plasmaspheric flux tube. The counterstreaming ion beams are the result of the expansion of the cold plasma from the conjugate ionospheres. Although the beams may excite several waves such as e-i and i-i acoustic waves and i-i eic waves, we have limited this study to the eic waves. The reason being that when highly supersonic ion beams begin to interpenetrate in the equatorial region of a flux tube, they are fast enough to excite eic waves and too fast for i-i acoustic modes. Therefore, so far as i-i interaction is concerned, the eic wave instability dominates during the early stage of the ion beam interpenetration. The subsequent phase of i-i oblique ion acoustic instability after the beams are slowed down is not included in this paper. The e-i interaction leads to electron heating. In the semikinetic model used here, electrons are assumed to obey the Boltzmann law and such heating is ignored. The eic interaction driven by the fast ion beams causes a perpendicular heating of ions. The heating leads to the generation of a warm anisotropic ion population, which first appears in the equatorial region and subsequently spreads all over the flux tube. In a narrow equatorial region the perpendicularly heated ions may have energies up to several tens of eV and they are highly anisotropic and locally trapped. The generation of the warm anisotropic ions significantly increases the equatorial plasma density.

Satellite observations show that equatorially trapped ions with large temperature anisotropies $T_{\perp} \gg T_{\parallel}$ commonly occur in the equatorial region [Olsen, 1981; Olsen *et al*, 1987]. A common explanation for the creation of such ions is perpendicular ion heating by waves driven by a tenuous hot plasma component. A commonly suggested wave mode is the fast magnetosonic wave which occurs at frequencies between the proton cyclotron frequency and the lower hybrid frequency [Curtis, 1985; Olsen *et al*, 1987]. However, a difficulty with this heating mechanism is that the cold ions do not resonate with the fast waves driven by the hot protons. We have shown here that the initially fast ion beams during the early stage of the refilling are a potential source of free energy for generating the equatorially trapped ions. These fast ions are the forerunners in the

expanding plasmas from the conjugate ionospheres into the initially empty flux tube [*Singh and Schunk*, 1983]. Such fast ions drive eic waves, which heats the beam ions perpendicularly. This heating leads to the generation of the anisotropic warm population (WAP) of ions all over the flux tube, but the highly anisotropic ions are confined to the equator. The non-equatorial WAP population in the region of relatively large plasma densities are subject to i-i Coulomb collisions and therefore may be eventually isotropized in several hours. On the other hand, the equatorially trapped ions are likely to isotropize in a much longer time due to (1) low equatorial density, and (2) the equatorial ions have the largest energies making Coulomb collisions less effective. In a future study such collisional effects will be rigorously examined by including them in the mesoscale model.

The observation of highly anisotropic trapped ions pertain to the equatorial region [*Olsen et al*, 1987]. On the other hand, the observation reported by *Sojka et al* [1983] revealed that the occurrence of anisotropic warm ions with pitch angle distribution peaking at 90° is also common in off-equatorial region on L shells ranging from that for the outer plasmasphere to that for the depleted magnetosphere. Specifically they reported that such warm anisotropic ions occur along with a thermal isotropic population inward of the plasmopause and outward they occur with field-aligned ion beams. It was found that as the satellite moved outward, the counterstreaming ion beams gave way to single beams coming from the closest ionosphere. Our simulation presented here corresponds to the situation just outside the of the plasmopause. In the simulations, singlestreaming ion beams are seen for relatively short duration which range from 1/2 to 1 hour as L increases from 4 to 6. On the other hand, the double streaming lasts for a relatively long time. Furthermore, in our simulations the doublestreaming is a prerequisite for the generation of warm anisotropic ions because the eic waves occur when the ion beams originating from the conjugate ionosphere begin to interpenetrate. Since singlestreaming is easily observed, it must be lasting over a fairly long time. This implies additional equatorial processes which are not included in the model. Such a process may be a continual loss of plasma from the flux tube from the equatorial region in the inner magnetosphere.

A continued refilling from bottom to top due to collision effects [*Wilson et al*, 1992] is likely to convert the relatively low energy field-aligned ions in a thermalized population, leaving the relatively more energetic WAP ions anisotropic. This suggests the production of the combination of TP and WAP ions observed on considerably filled flux tubes [*Sojka et al*, 1983]. However, this remains to be rigorously modeled.

Our present model reveals a mechanism of creating the warm anisotropic plasma all along the flux tube. We reiterate that such ions are generated primarily in the equatorial region and subsequently they spread all over the flux tube by the field-aligned flow. Further evolution of the WAP population due to Coulomb collisions will be the subject of a future study. But simple calculations based on Coulomb collision time show that the WAP ions created during the early stage refilling last for a sufficiently long time to be easily observable. Their life time ranges from about 10 hours at high latitudes to several days in the equatorial region.

Acknowledgment: This work was supported by NASA grant NAGW-2128, and NSF grant ATM 9301024.

References

- Banks, P. M., A. F. Nagy, and W. I. Axford, Dynamical behavior of thermal protons in the mid-latitude ionosphere and magnetosphere, *Planet. Space Sci.*, **19**, 1053, 1971.
- Brown, D. G., G. R. Wilson, J. L. Horwitz, and D. L. Gallagher, Self-consistent productions of ion conics on return current region auroral field lines: A time-dependent, semi-kinetic model, *Geophys. Res. Lett.*, **18**, 1841, 1991.
- Curtis, S. A., Equatorial trapped plasmasphere ion distributions and transverse stochastic acceleration, *J. Geophys. Res.*, **84**, 2597, 1985.
- Davidson, R. C., *Methods in Nonlinear Plasma Theory*, Academic Press, New York, 1972.
- Foote, E. A., and R. M. Kulsrud, Stability of colliding ion beams, *Phys. Fluids*, **24**, 1532, 1981.
- Forslund, D. W., and C. R. Shonk, Numerical simulation of electrostatic counterstreaming instabilities in ion beams, *Phys. Rev. Lett.*, **25**, 281, 1970.
- Fujita, T., T. Ohnuma and S. Adachi, Self-oscillations excited by two stream ion-ion instability, *Plasma Phys.*, **19**, 875, 1977.
- Ganguli, S. B., and P. J. Palmadesso, Plasma transport in the auroral return current region, *J. Geophys. Res.*, **92**, 8673, 1987.
- Gary, S. P., M. E. McKean, D. Winske, G. J. Anderson, R. E. Denton, and S. A. Fuselier, The proton cyclotron instability and the anisotropy/B inverse relation, *J. Geophys. Res.*, **99**, 5903, 1994.
- Lin, J., J. L. Horwitz, D. L. Gallaher, and C. J. Pollock, The streaming-trapped ion interface in the equatorial inner magnetosphere, *J. Geophys. Res.*, **100**, in review, 1995.
- McKee, C. F., Simulation of counterstreaming plasmas with application to collisionless electrostatic shocks, *Phys. Rev. Lett.*, **18**, 990, 1970.
- Olsen R. C., Equatorially trapped plasma populations, *J. Geophys. Res.*, **86**, 11,235, 1981.
- Olsen R. C., C. R. Chappell, D. L. Gallagher, J. L. Green and R. R. Anderson, Plasma observations at the magnetic equator, *J. Geophys. Res.*, **92**, 2385, 1987.

- Rasmussen, C. E., and R. W. Schunk, Multistream hydrodynamic modeling of interhemispheric plasma flow, *J. Geophys. Res.*, 93, 14,557, 1988.
- Schulz, M., and M. C. Koons, Thermalization of colliding ion streams beyond the plasmapause, *J. Geophys. Res.*, 77, 248, 1972.
- Singh, N., Ion-Electron instability of ion-beam-plasma systems, *Physics Letters*, 67A, p. 372, 1978.
- Singh, N., Role of ion temperature anisotropy in multistage refilling of the outer plasmasphere, *Geophys. Res. Lett.*, 18, 817-820, 1991.
- Singh, N., and L. C. Leung, Numerical simulation of filling a magnetic flux tube with a cold plasma: Anomalous plasma effects, *J. Geophys. Res.*, 100, 3585, 1995.
- Singh, N., and R. W. Schunk, Numerical simulations of counterstreaming plasmas and their relevance to interhemispheric flow, *J. Geophys. Res.*, 88, 7867, 1983.
- Singh, N., R. W. Schunk, and H. Thiemann, Temporal features of the refilling of a plasmaspheric flux tube, *J. Geophys. Res.*, 91, 13433, 1986.
- Singh, N., G. R. Wilson, and J. L. Horwitz, Comparison of hydrodynamic and semikinetic treatments for a plasma flow along closed field lines, *J. Geophys. Res.*, 99, 11,495, 1994.
- Sojka, J. , R. W. Schunk, J. F. Johnson, J. H. Waite, and C. R. Chappell, Characteristics of thermal and superthermal ions associated with the dayside plasma trough as measured by the Dynamics Explorer retarding ion mass spectrometer, *J. Geophys. Res.*, 88, 7895, 1983.
- Wilson, G. R., J. L. Horwitz, and J. Lin, A semikinetic model for early stage plasmasphere refilling, 1, Effects of Coulomb collisions, *J. Geophys. Res.*, 97, 1189, 1992.

FIGURE CAPTIONS:

Fig. 1. Marginal stability diagram for symmetric counterstreaming ion beams (see insert) in a plasma with a magnetic field. V_{tb} is the beam thermal velocity. For $V_b / \sqrt{2} V_{tb} \lesssim 3$ the i-i acoustic mode dominates and for $V_b / \sqrt{2} V_{tb} > 3$ the eic mode dominates.

Fig. 2. Geometry of the mesoscale model. A flux tube with dipolar magnetic field is simulated from $\lambda = -\lambda_o$ to $\lambda = \lambda_o$. The distance S is measured from $S = 0$ at $\lambda = \lambda_o$ to $S = S_{\max}$ at $\lambda = -\lambda_o$.

Fig. 3. Evolution of ion flow in a flux tube with $L = 4$. Phase space plots in the $S - V_{\parallel}$ plane at some selected times. S is the distance from the northern hemispheric boundary at $\lambda = \lambda_o = 57.5^\circ$.

Fig. 4. Beam velocity and temperature distributions along the flux tube for the beam originating from the northern ionosphere. (a) Beam velocity normalized to the thermal velocity $V_{iH} = (k_B T_o / m_i)^{1/2}$. (b) Parallel temperature. (c) Beam velocity normalized to the local thermal velocity $V_{it} = (k_B T / m_i)^{1/2}$. Note the large beam velocities relative to V_{it} in the equatorial region.

Fig. 5. Evolution of ion flow with eic wave heating. Left and right hand columns show the $S - V_{\parallel}$ and $S - V_{\perp}$ phase space at some selected times. Note the appearance of perpendicularly heated ions in the equatorial region at early times $t \leq 30$ minutes, and their subsequent spread all over the flux tube.

Fig. 6. Velocity distribution functions in the equatorial region ($|\lambda| \leq 10^\circ$) at $t = 4$ hours. (a) $F(V_{\parallel})$ and (b) $F(V_{\perp})$. The perpendicular distribution shows two distinct populations, a cold core and a warm component.

Fig. 7. Distribution of equatorial ions in the $V_{\perp} - V_{\parallel}$ plane. (a) $|\lambda| \leq 10^\circ$. Note the presence of beam ions, a warm anisotropic population, and a loss cone. (b) $30^\circ < \lambda < 45^\circ$, (c) $45^\circ < \lambda < 57.5^\circ$. Note the merging of the ion beams in (c).

Fig. 8. Evolution of ion density profile as a consequence of flux tube refilling. Note that the refilling saturates in a few hours.

Fig. 9. Comparison of the saturated density profiles with and without the eic wave heating. The eic wave heating leads to a higher equatorial density.

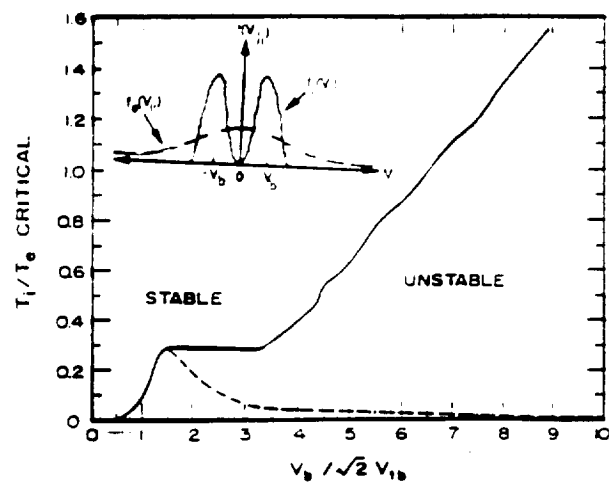


Fig. 1

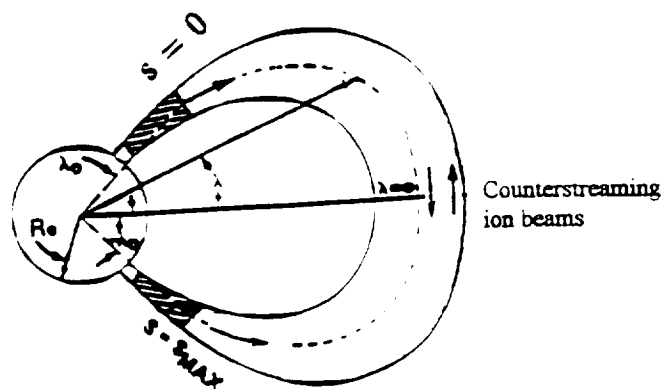


Fig.2

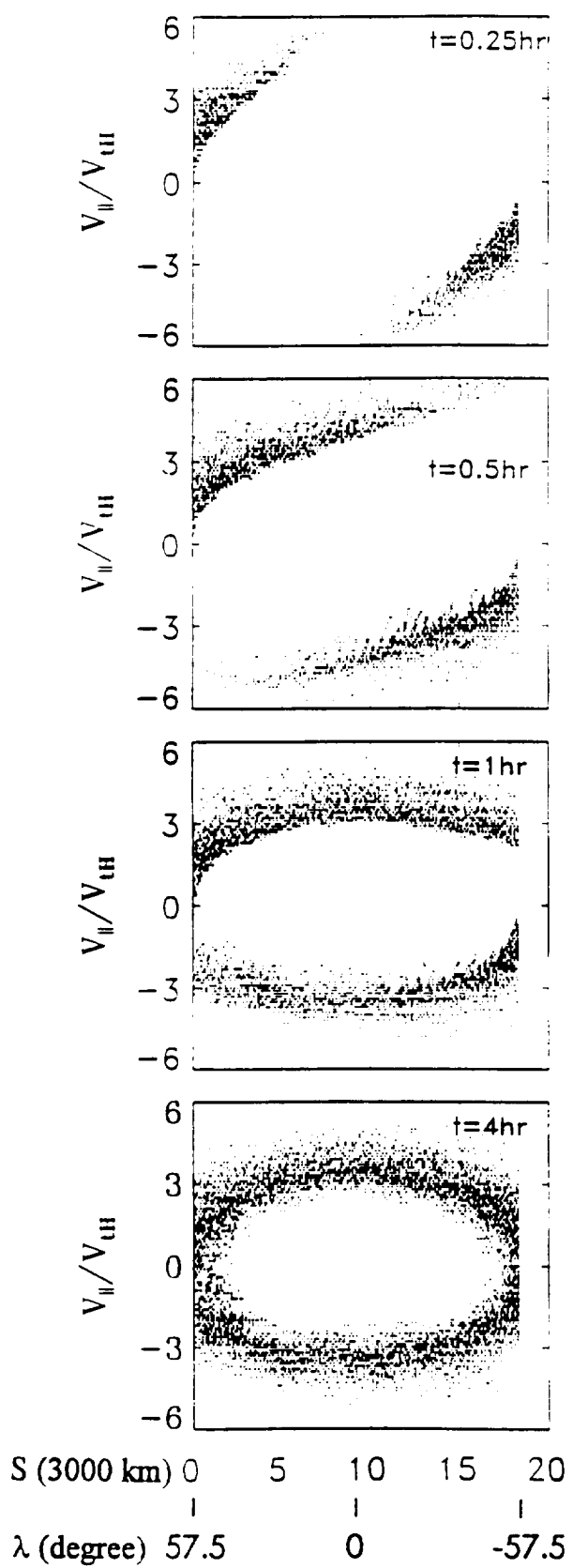


Fig. 3

$t = 30 \text{ min}$

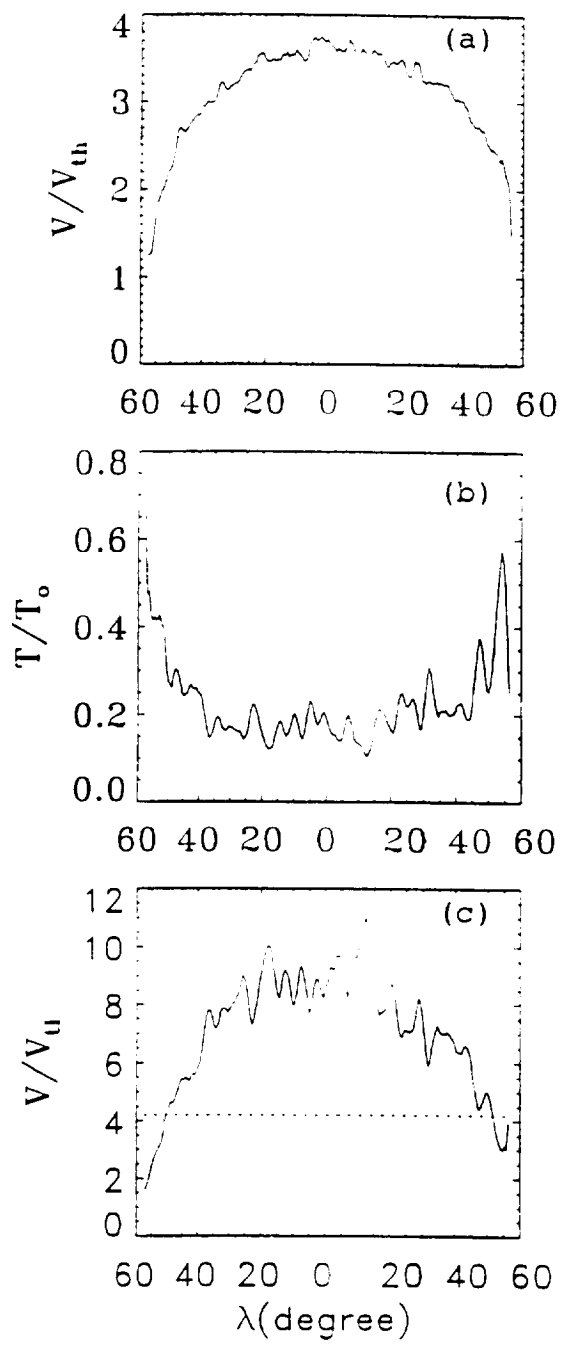


Fig. 4

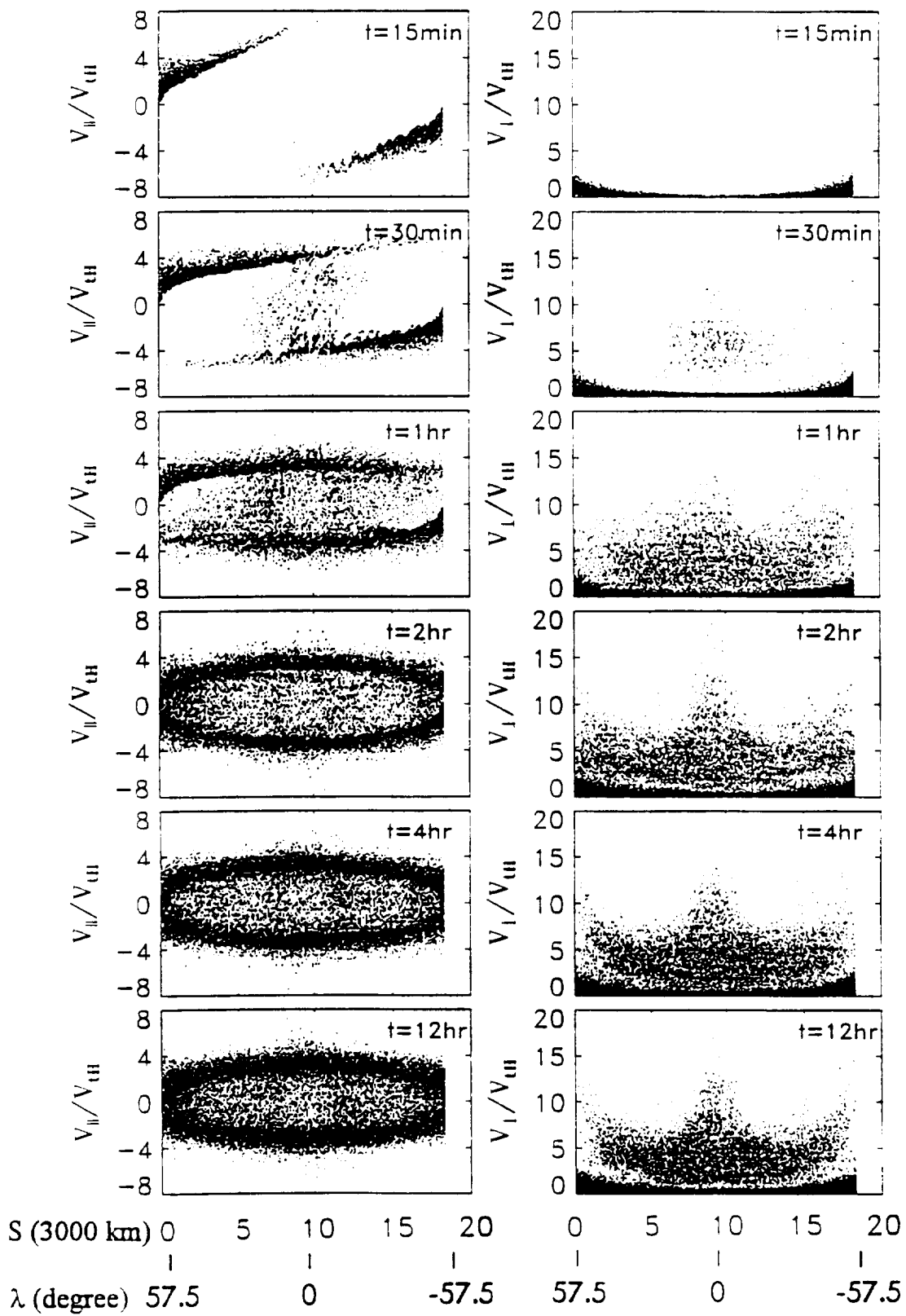


Fig. 5

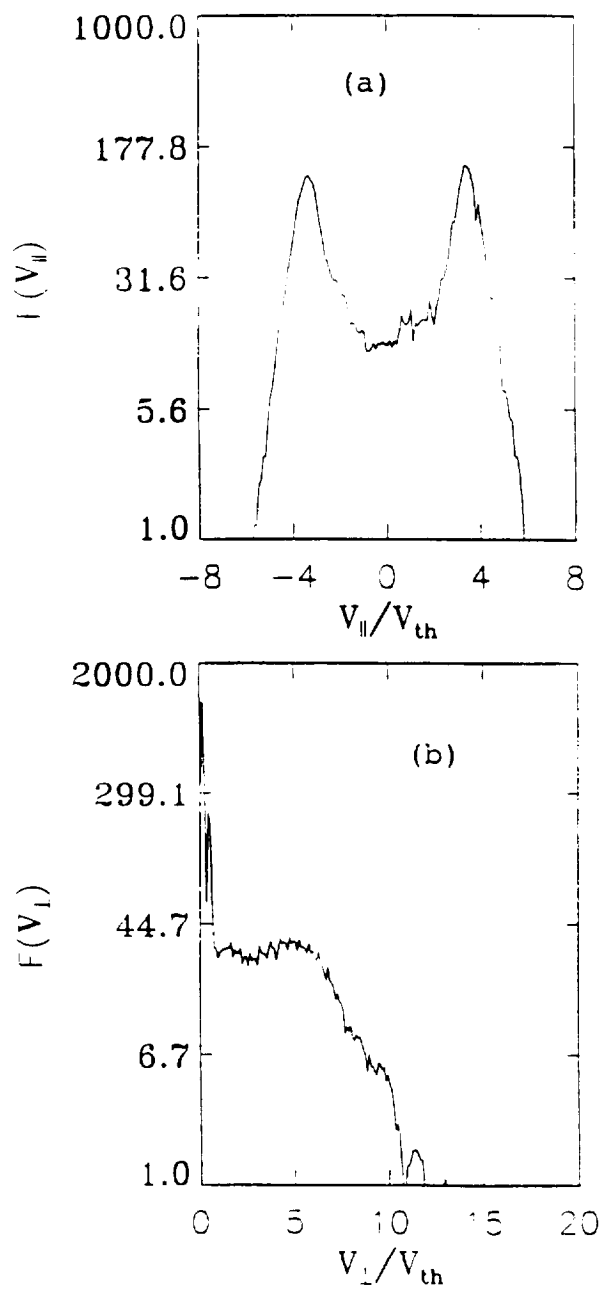


Fig. 6

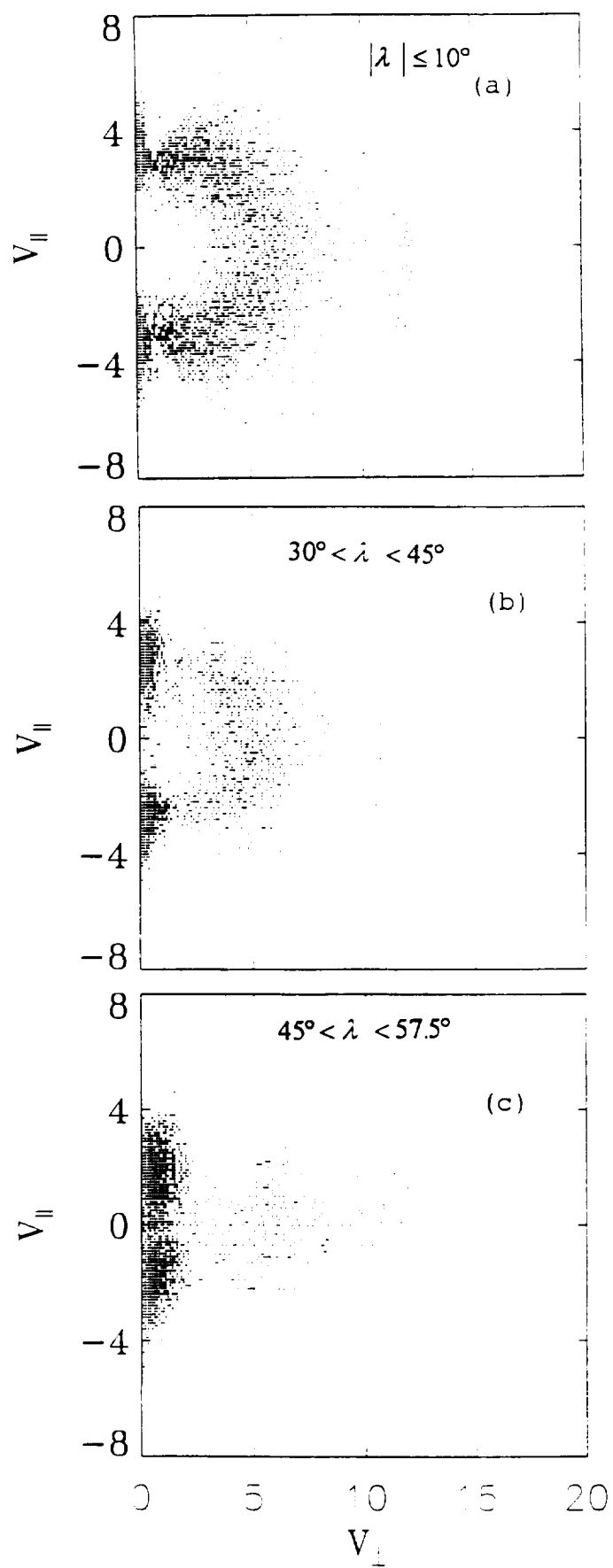


Fig. 7

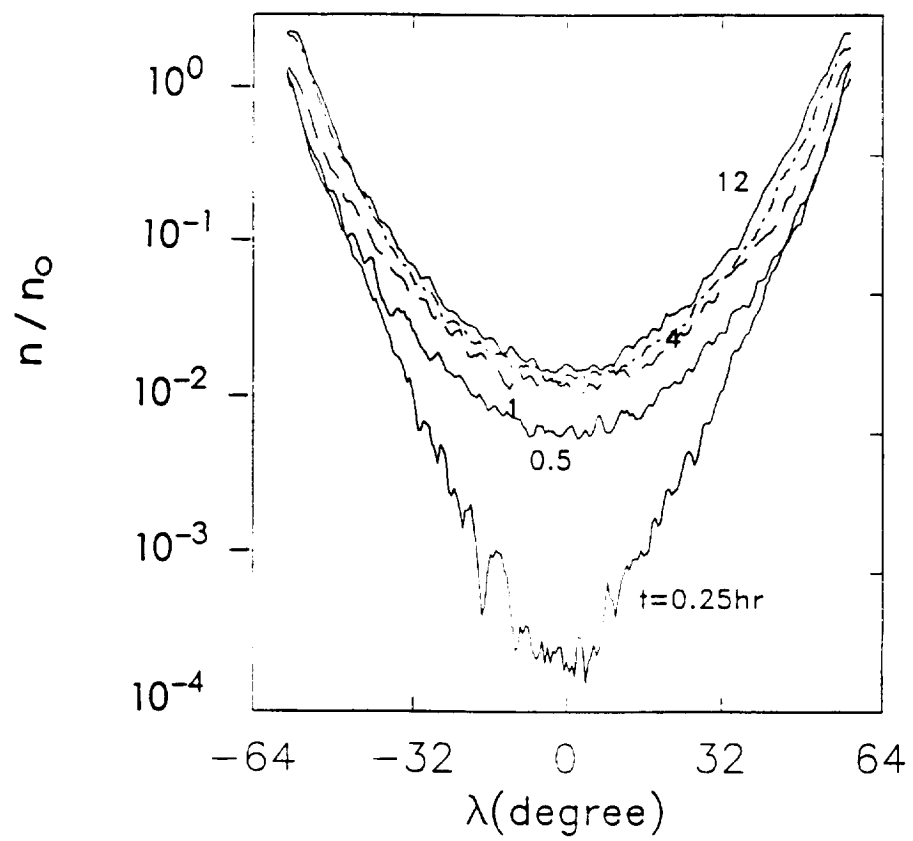


Fig. 8

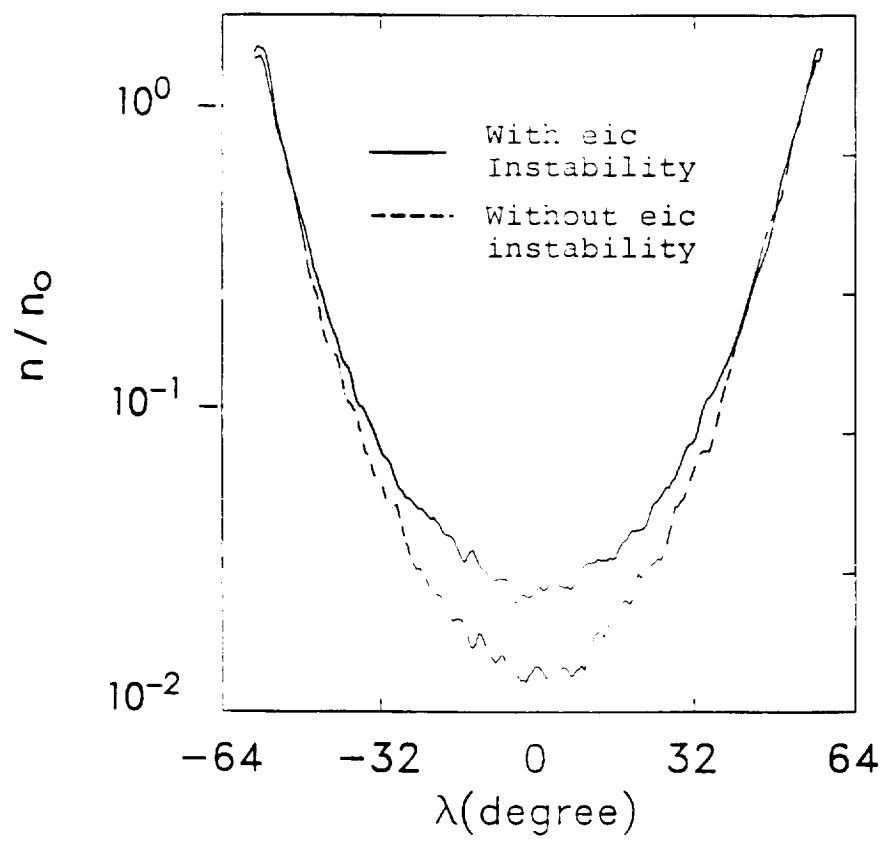


Fig. 9

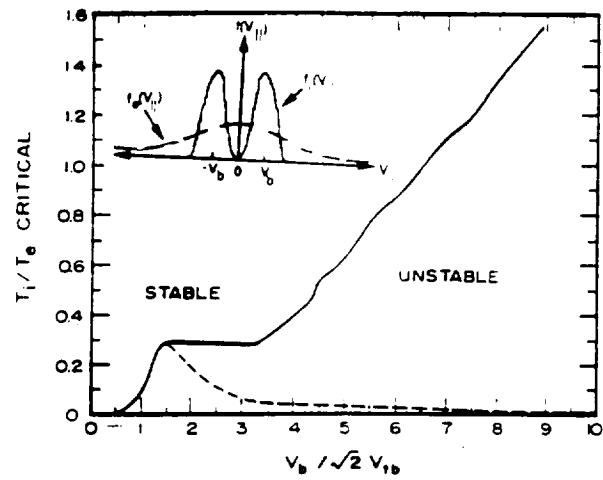


Fig. 1

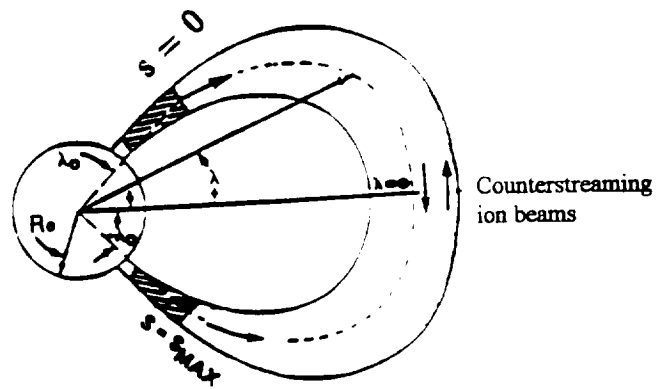


Fig.2

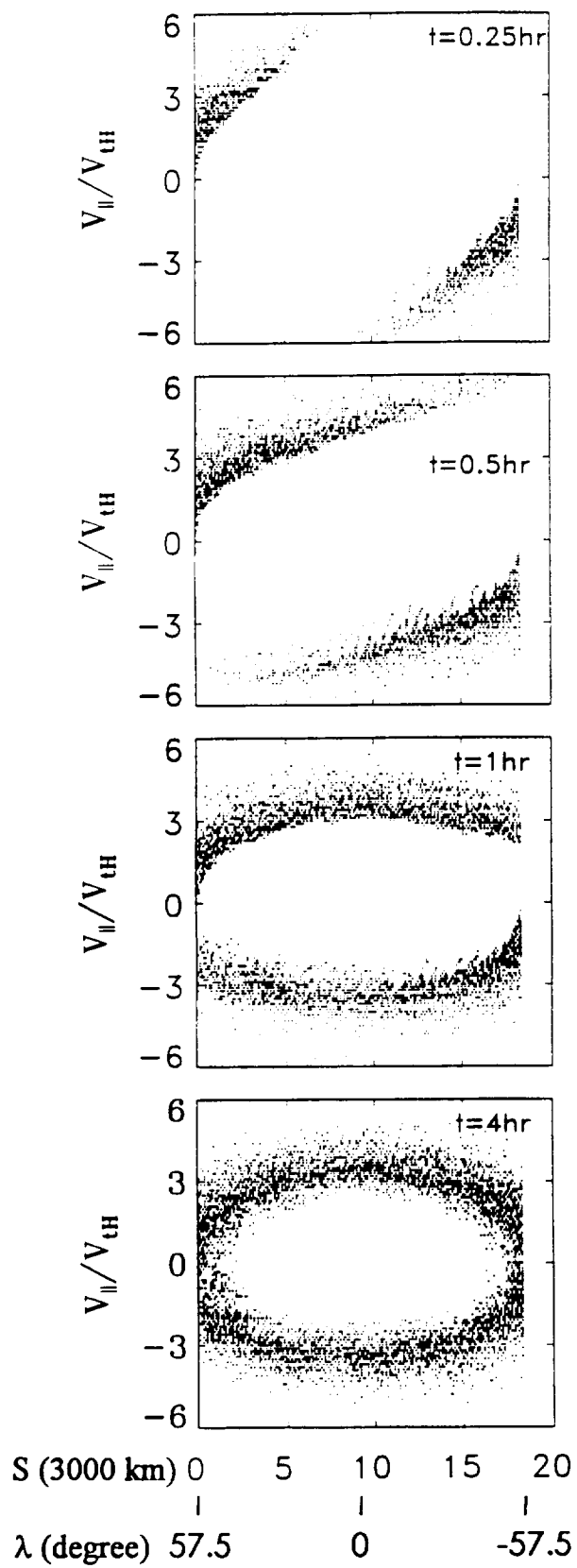


Fig. 3

$t = 30 \text{ min}$

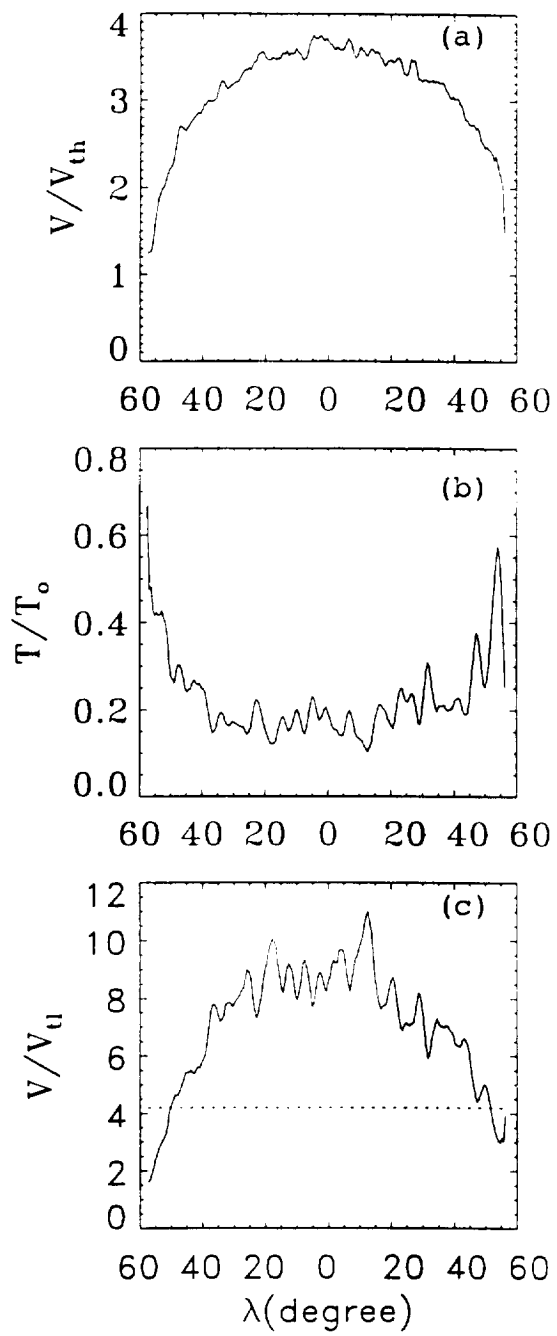


Fig. 4

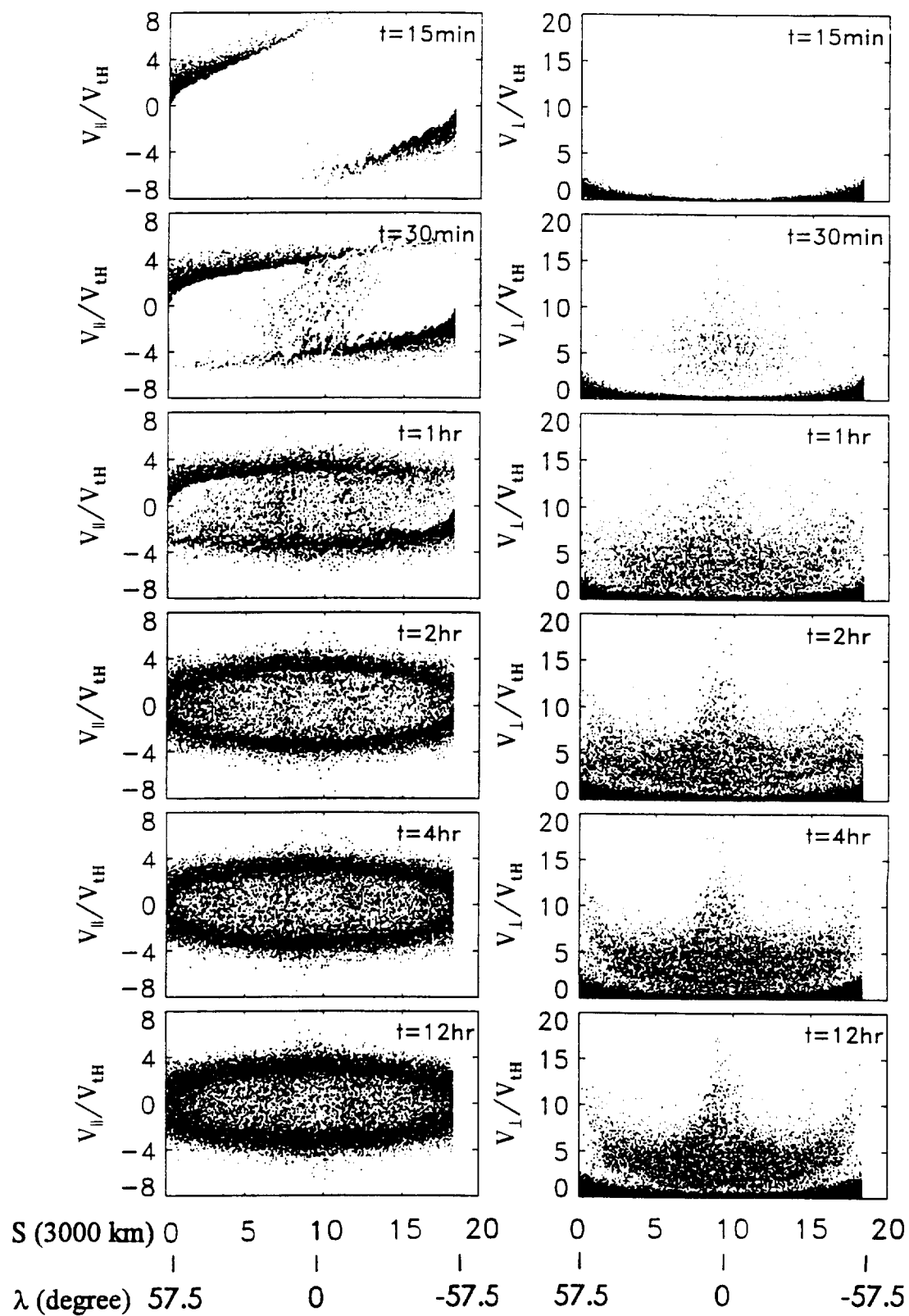


Fig. 5

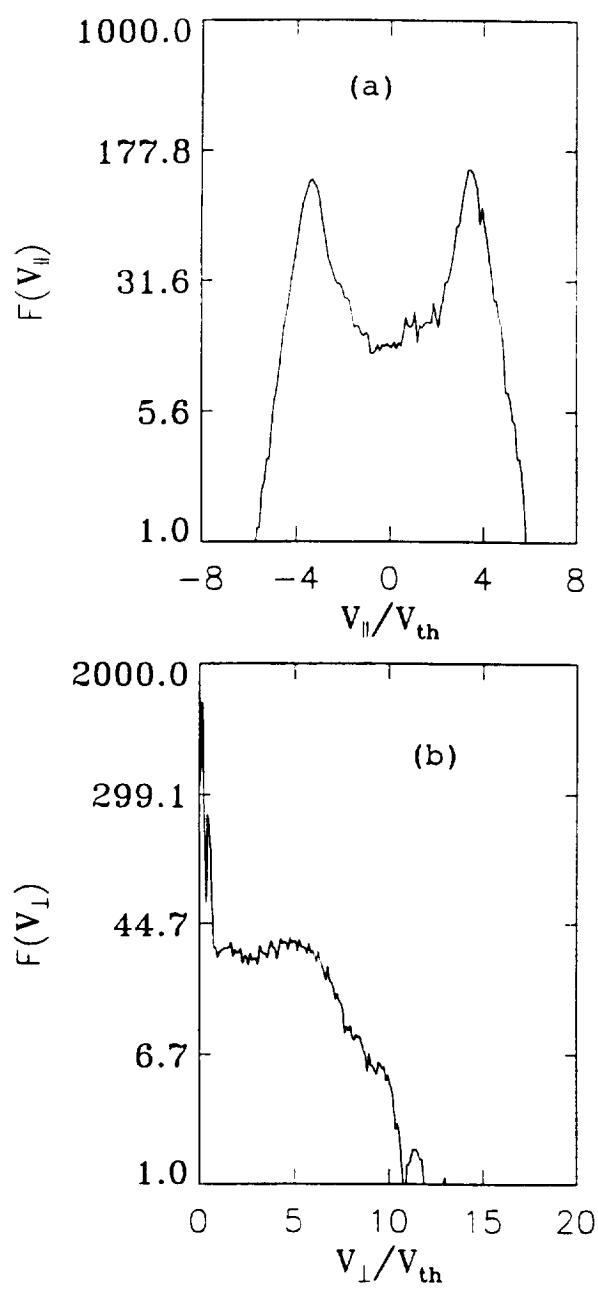


Fig. 6

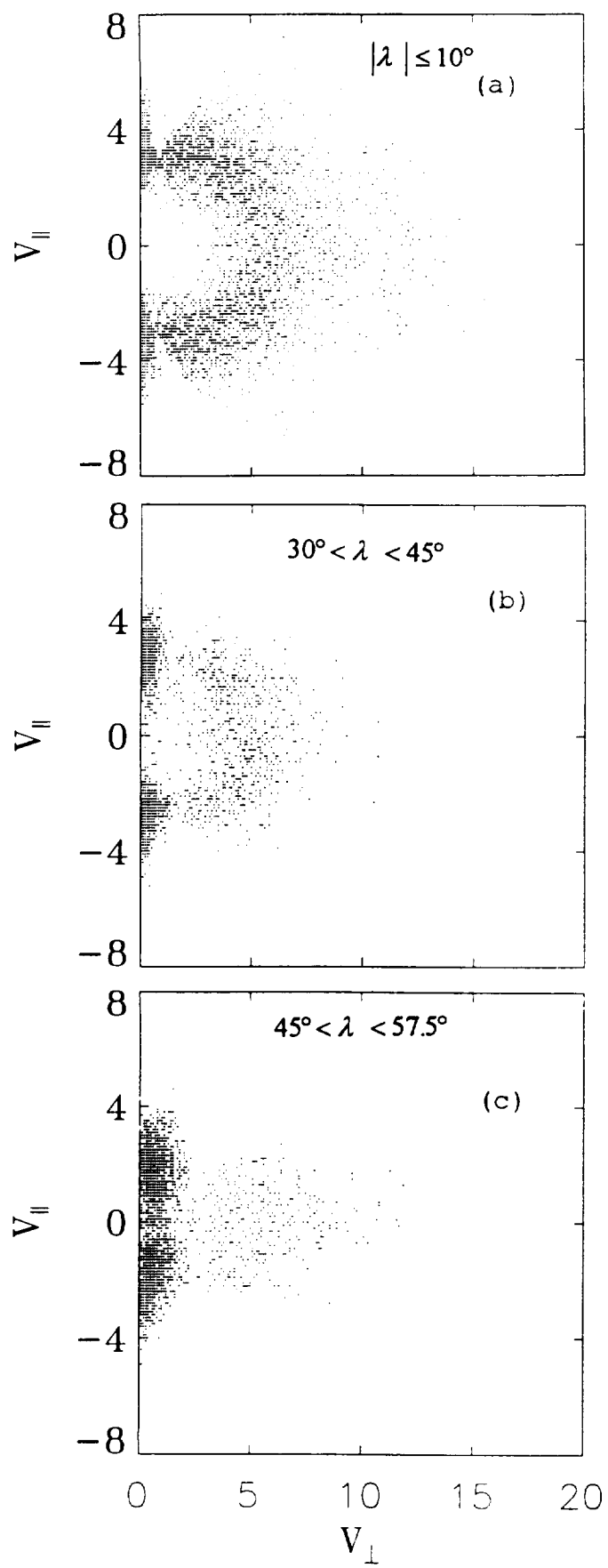


Fig. 7

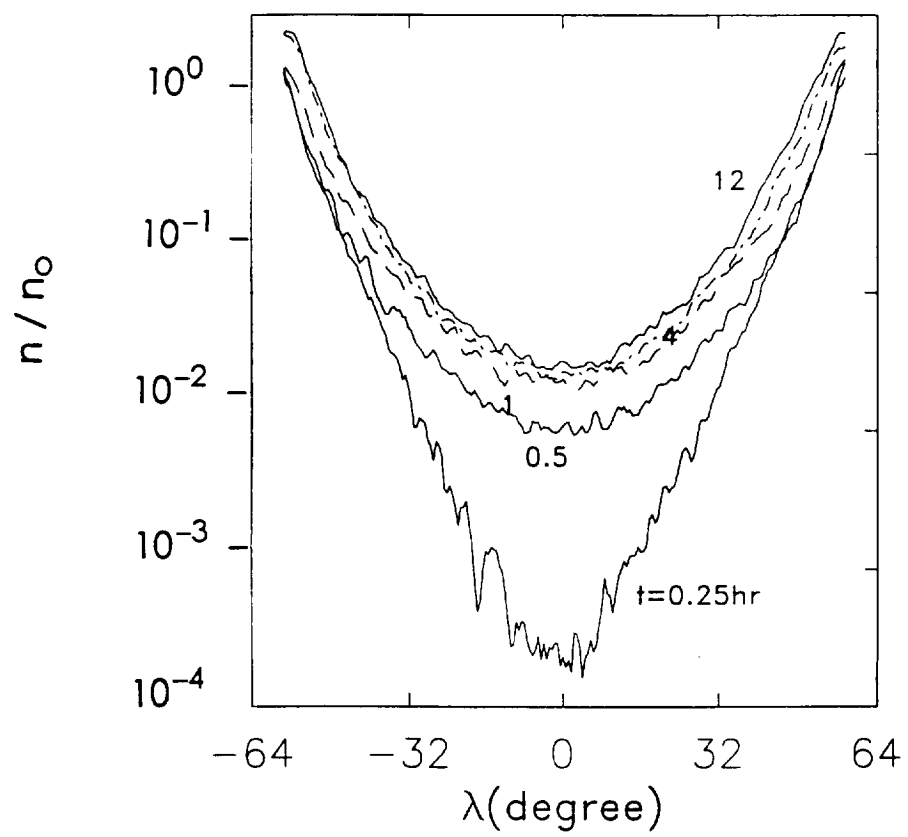


Fig. 8

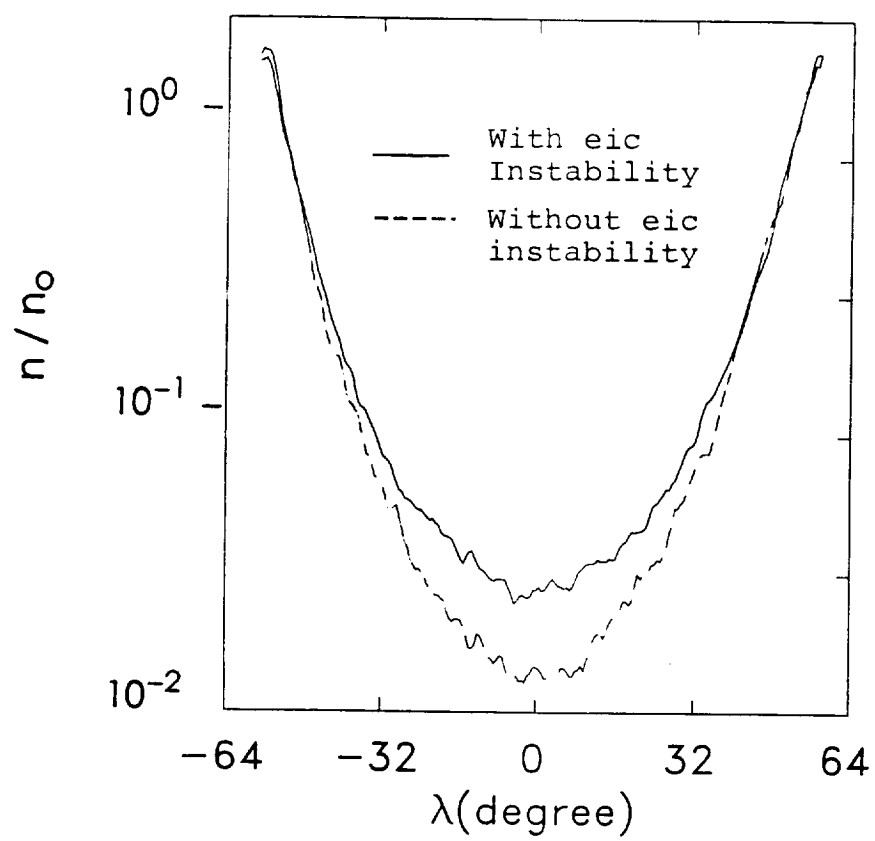


Fig. 9